Batteries & Supercaps

Research Article
doi.org/10.1002/batt.202500704

Chemistry Europe
European Chemical Societies Publishing

www.batteries-supercaps.org

Modeling and Simulation of an Alkaline Ni/Zn Cell

Felix K. Schwab,* Britta Doppl, Niklas J. Herrmann, Alice Boudet, Shadi Mirhashemi, Sylvain Brimaud, and Birger Horstmann*

Nickel/zinc (Ni/Zn) batteries are a promising post-lithium technology for stationary energy storage applications offering advantages in safety, environmental compatibility, and resource availability. Although this battery chemistry has been known for decades, the theoretical knowledge about its electrochemical processes remains limited. In order to gain a deeper understanding of the general cycling behavior and the underlying processes, but also specific phenomena intrinsic to zinc-based cells such as zinc shape change, simulations based on a thermodynamically consistent, volume-averaged continuum model are performed. A Ni/Zn prototype cell is used as a reference framework to provide a basis for modeling, parameter estimation, and systematic comparison between simulated and experimental cell behavior to enhance cyclability and performance.

1. Introduction

Zinc-metal batteries come with a beneficial set of properties, which—in principle—enables them to compete with the nowadays widespread lithium-ion batteries, especially in stationary applications. There, when weight is not the only criterion for a successful utilization, zinc electrodes convince with a rather high theoretical capacity (819.7 mAh g^{-1}) and relative stability against corrosion in aqueous electrolytes.[1] The usage of such electrolytes significantly lowers their environmental harm, toxicity, and flammability, which predestines them to areas where high safety regulations apply, while their conductivity is high.[2,3] Both zinc and aqueous electrolytes are typically low-cost.

These appealing characteristics reflect in a long-standing and ongoing interest in this technology, which has resulted in a whole family of zinc-metal batteries,[1,2,4,5] e.g., Zn/Ni, Zn/Air, Zn/MnO_2, or Zn/Ag, amongst others. But despite this continuous research effort,[6,7] certain processes such as the redistribution of zinc—the so-called shape change, densification, and passivation, dendrite formation or hydrogen formation persist,[5,8–11] regardless of a better understanding and progress with these topics.

A promising electrode pair is Zn/Ni (in the following the more usual term Ni/Zn is used), which makes use of the well-established β-NiO(OH)/β-$Ni(OH)_2$ insertion material as the positive electrode that is stable in alkaline media.[12] When this element combination is constructed as a vented battery, high energy and power densities[12–14] and cycle life at good depths of discharge (DoD)[15,16] may be achieved. The theoretical capacity of the positive electrode (289.1 mAh g^{-1}) is the limit for the cell,[12] which may be maximally utilized to up to around 90% due to oxygen formation at the end of charge.[17,18]

Along with the history of zinc metal batteries, efforts to model them on a continuum scale date back a long time. Numerous modeling works can be found for the stand-alone zinc electrode, or in any combination (see refs. [6,19,20], amongst others). Important topics have been the correct description of the Zn/ZnO dissolution-precipitation reaction,[21–23] hydrogen formation,[24] the change in active surface area due to zinc conversion and hindered transport through the ZnO porous layer.[23,25–27] Equally, the β-NiO(OH)/β-$Ni(OH)_2$ electrode has been extensively modeled, mostly in the context of Ni/Cd or metal-hydride batteries, see refs. [28,29], amongst others. Here, the electrode's open-circuit potential (OCP) curve and hysteresis,[30–32] the proton insertion modeled as solid diffusion[33,34] and the oxygen formation at the end of charge[30–32] have been of importance. In the case of Ni/Zn continuum models, only a few works exist. In an early one, Choi and Yao[35] examined the cell type with a focus on the Ni electrode, already including the convection of the electrolyte solution but neglecting the O_2 formation. The influence of operating conditions, e.g., the rate of charge and species

F. K. Schwab, B. Doppl, N. J. Herrmann, B. Horstmann
Institute of Engineering Thermodynamics - Computational Electrochemistry
German Aerospace Center (DLR)
Wilhelm-Runge-Str. 10, 89081 Ulm, Germany
E-mail: felix.schwab@dlr.de
birger.horstmann@dlr.de

F. K. Schwab, B. Doppl, N. J. Herrmann, B. Horstmann
Helmholtz Institute Ulm (HIU)
Helmholtzstr. 11, 89081 Ulm, Germany

A. Boudet, S. Mirhashemi
SunErgy
85-93 Boulevard Alsace-Lorraine, 93115 Rosny-sous-Bois, France

S. Brimaud
Zentrum für Sonnenenergie- und Wasserstoff-Forschung
Baden-Württemberg (ZSW)
Helmholtzstr. 8, 89081 Ulm, Germany

B. Horstmann
Faculty of Natural Science
Ulm University
Albert-Einstein-Allee 11, 89069 Ulm, Germany

Supporting information for this article is available on the WWW under https://doi.org/10.1002/batt.202500704

Research Article
doi.org/10.1002/batt.202500704
Chemistry Europe
European Chemical Societies Publishing

concentrations, on the charge acceptance of the electrode is described. Miller et al.[36] analyzed concentration levels in the whole extent of the cell. Isaacson et al.[37] used a 2D continuum model to investigate concentration and current density distribution, the zinc shape change and the influence of an electrolyte reservoir. Again, O_2 formation and other aspects of the Ni electrode are not part of the model due to an emphasis on the Zn electrode. Later, Arise et al.[38,39] used a simplified model to study transient concentration profiles in the cell and to explain experimentally found morphology changes in the Zn electrode, without, e.g., accounting for the zinc dissolution-precipitation reactions. Huang et al.[40] used a continuum model to assist the development of new nickel high-power electrodes. The model includes O_2 formation and solid diffusion proton insertion.

The aim of this study is to present a 3D model of a Ni/Zn cell, which is able to represent the experimental data of such a cell prototype. For this purpose, we combine the relevant aspects of the Ni/Zn technology in one continuum model, focusing on dissolution-precipitation at the Zn electrode as well as proton insertion and O_2 formation at the Ni electrode. Concentrated solution theory for the electrolyte solution, including convection completes the model. On this basis, we discuss, evaluate, and compare the predictions of the cell model to experimental results and images. The modeling is based on the work of Latz and Zausch,[41,42] who introduced a thermodynamically consistent transport theory for lithium-ion batteries. Aspects of the Zn electrode are mainly based on works of Stamm et al.[26] and Schmitt et al.,[27] while the model for the Ni electrode is largely inspired by preliminary work by Doppl,[43] which is based on Paxton and Newman[29] and Albertus et al.[32]

Before stating our computational and experimental methods in the upcoming section, we formulate the reactions which drive the alkaline Ni/Zn cell and describe the battery's working principle.

Main working principle and reactions When discharging the Ni/Zn cell, the following happens: First, at the negative Zn/ZnO electrode, zinc is dissolved and released into the strongly alkaline ZnO-saturated KOH electrolyte solution as $Zn(OH)_4^{2-}$ (zincate, **Figure 1**(I)) while providing two elect,

$$Zn + 4\,OH^- \rightleftharpoons Zn(OH)_4{}^{2-} + 2\,e^- \quad (1)$$

with $\Delta\phi^\circ = -1.20$V/SHE. Continued dissolution and redeposition of Zn change the shape of the electrode. As seen in Reaction (1), this process requires OH^- (hydroxide) ions, which are transported through the separator coming from the positive β-NiO(OH)/β-$Ni(OH)_2$ electrode. Second, the electrons stemming from the zinc dissolution arrive through the electric circuit and split the water in the electrolyte solution (Figure 1(II)). The emerging protons are inserted into the NiO(OH) structure,

$$\beta\text{-}NiO(OH) + H_2O + e^- \rightleftharpoons \beta\text{-}Ni(OH)_2 + OH^- \quad (2)$$

with $\Delta\phi^\circ = +0.49$ V/SHE, and the OH^- ions transported to the negative electrode close the circuit. Lastly, when the zincate concentration in the electrolyte solution rises above its saturation limit, a precipitation reaction takes place, forming a ZnO layer on top of the Zn in the negative electrode (Figure 1(III)),

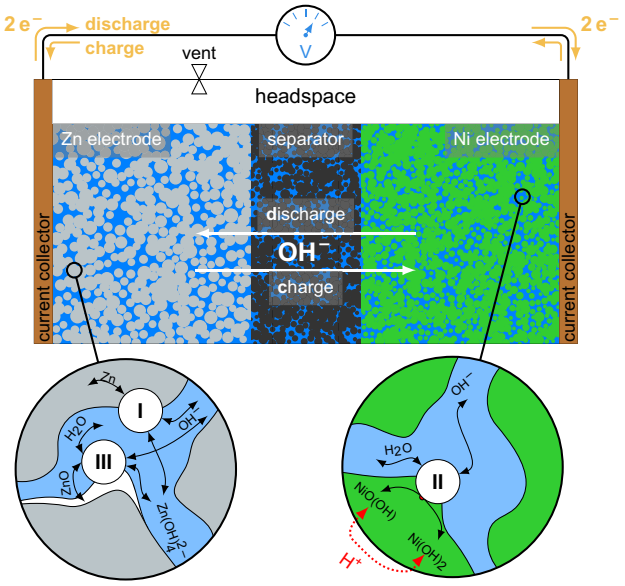

Figure 1. Schematic representation of a vented Ni/Zn cell together with the most important reactions.

$$Zn(OH)_4{}^{2-} \rightleftharpoons ZnO + H_2O + 2\,OH^- \quad (3)$$

This is an important part of the battery concept, as the precipitation allows Reaction (1) to continue efficiently through $Zn(OH)_4^{2-}$ being stored compactly as ZnO. However, this precipitation often forms a passivating layer on Zn surfaces. When charging, all these processes are reversed. Overall, the cell reaction is

$$Zn + 2\,\beta\text{-}NiO(OH) + H_2O \rightleftharpoons ZnO + 2\,\beta\text{-}Ni(OH)_2 \quad (4)$$

with $\Delta\phi^\circ = +1.69$ V/SHE.

Due to the cell voltage, which lies outside the electrochemical stability window of water, $\Delta E = 1.23$ V, two side reactions, hydrogen and oxygen evolution reactions (HER and OER), play a major role

$$2\,H_2O + 2\,e^- \rightleftharpoons H_{2(aq)} + 2\,OH^- \quad (5)$$

$$4\,OH^- \rightleftharpoons 2\,H_2O + O_{2(aq)} + 4\,e^- \quad (6)$$

with $\Delta\phi^\circ = -0.83$ V/SHE and $\Delta\phi^\circ = +0.40$ V/SHE, respectively. The main consequence of the OER is a reduced Coulombic efficiency (CE), which in turn leads to more ZnO being dissolved during charging than is precipitated during discharging. However, this ZnO imbalance is counteracted by a portion of the O_2 produced being transported from the Ni electrode through the separator to the Zn electrode, where it reacts to form ZnO,[5,17]

$$2\,Zn + O_{2(aq)} \rightleftharpoons 2\,ZnO \quad (7)$$

Excess O_2 and H_2 are released from the electrolyte through Reaction (S7) and (S8), see Section S9, Supporting Information. In such cells, but disregarded in this work, these gases are

collected in a headspace (see Figure 1), which serves additionally as an electrolyte reservoir. There, the gases recombine to water at a catalyst or vent through a valve when pressure becomes critical.[5,8,12,17,18] This causes loss of electrolyte solution, which may result in a so-called dry-out,[5] leaving parts of the electrodes non-wetted. Occasional electrolyte refilling may be required.

Structure In the following, we will give details on the computational and experimental methods used, pointing out the important aspects of the transport and reaction modeling. Then, in the results and discussion section, we present findings from the simulation of single cycles and long-term cycling. They are compared to experimental results, discussed and optimization strategies are outlined. Lastly, we give a summary and a conclusion of our work.

2. Computational and Experimental Methods

We conducted experiments and computational studies on the basis of a vented Ni/Zn cell with a strongly alkaline KOH electrolyte solution. It hence combines a conversion-type Zn electrode, which dissolves during the discharge process, with an insertion-type Ni electrode, which stores protons. Due to the use of an aqueous electrolyte solution and operation outside of the electrochemical stability window of water, gases are produced, affecting battery functioning.

Regarding the cell model, the most important assumptions and approaches are derived from the description in the introductory paragraph on working principles and reactions, which will only be discussed in essence here. For further details, we refer the interested reader directly to the Supporting Information.

2.1. Modeling Approach

The main functionality of a battery cell, the conversion of chemical to electric energy through electrochemical reactions, happens at the interfaces between the solid electrodes and an electrolyte solution. Furthermore, the transport of electrons through the former and ions through the latter has to be ensured to close the circuit. In order to represent this behavior in a consistent physicochemical model, a physics-based model approach is chosen that includes the transport process in the form of balance equations and reactions as (electro-) chemical kinetics. Based on similar and already existing models for lithium-based or zinc-based batteries, the Ni/Zn cell discussed here is modeled.[26,27,41,42] In the following, only the basic assumptions and foundation of our model will be introduced. We will not list and explain the numerous model equations and parameters in detail here, but refer the interested reader to the Supporting Information.

2.1.1. Transport in Electrolyte and Electrodes

Two crucial assumptions form the basis of our transport description. First, the strongly alkaline electrolyte solution requires the use of concentrated solution theory, which introduces transport parameters that are independent of each other.[26] For each species k in the electrolyte solution, we have a diffusion coefficient D^k, a transference number t^k, and for the solution in total an ionic conductivity κ. Second, we use a volume-averaged description to circumvent a detailed representation of the electrodes' and the separator's microstructure,[27] which helps to make a 3D simulation of a whole battery cell feasible. Volume averaging condenses the microstructure information of a phase α, e.g., solid electrode phase or liquid electrolyte phase, into two phase-specific quantities, volume fraction ε^α and tortuosity τ^α. In each point, the volume fractions of all solids, liquids, and gases have to follow the sum constraint $\varepsilon^s + \varepsilon^l + \varepsilon^g = 1$. On an abstract level, this leads then to effective parameters and quantities, e.g., effective diffusion coefficients $D^{k,\text{eff.}} = {}^{\varepsilon}/_{\tau}D^k$ or effective concentrations $c^{k,\text{eff.}} = \varepsilon c^k$, which has the microstructure information inscribed.

Within this framework, a major part is the transport or balance laws in each phase. In the liquid electrolyte phase, these transport equations comprise fluxes due to diffusion, electromigration, and volume-centered convection. While diffusion and electromigration are caused by gradients in concentrations and electric potential, respectively, convection in our model roots from changes in the solid and liquid volume fractions, inducing a pressure in the liquid, p^l, causing a displacement of liquid.[27] Here, the volume-centered description[44,45] is used instead of the mass-centered one to facilitate the evaluation of the incompressibility condition. These coupled fluxes then drive the transport of species in the electrolyte solution, which are represented by local concentrations c^k, $k = \{OH^-, Zn(OH)_4^{2-}, O_{2(aq)}, H_{2(aq)}\}$, and allow for their temporal and spatial evolution. Furthermore, we solve for the electrolyte potential ϕ^e. The resulting concentration balances and charge conservation in the electrolyte solution are then written as

$$\begin{aligned} \frac{\partial \varepsilon^l c^k}{\partial t} &= -\vec{\nabla}\cdot\left(\vec{N}^{k,\text{eff}} + \varepsilon^l c^k \vec{v}\right) + \sum_r A^r \nu^{kr} j^r \\ 0 &= -\vec{\nabla}\cdot\left(\vec{j}^{\text{el,l,eff}}\right) + \sum_r A^r F z^r j^r \end{aligned} \tag{8}$$

where $\vec{N}^{k,\text{eff}}$ and $\vec{j}^{\text{el,l,eff}}$ represent the effective particle flux and ionic current densities, respectively, which are defined in Equation (S8) and (S9), Supporting Information. The convection is driven by the volume-centered velocity $\vec{v}$, and the source terms summing over all relevant reaction r comprise the reaction-specific surface area A^r, the number of transferred electrons z^r, the Faraday constant F, the reaction rate j^r and the corresponding stoichiometric coefficient ν^{kr}. In the solid phases of the electrodes, only electronic conduction plays a role, which is caused by the gradient of the solid phase (electrode) potential ϕ^s.

The difference between ϕ^s and ϕ^e drives electrochemical reactions at the electrode–electrolyte interfaces, which are modeled as phenomenological Butler–Volmer equations giving the reaction rates j^r of the source terms in Equation (8). If $O_{2(aq)}$ and $H_{2(aq)}$ oversaturate in the electrolyte solution, they outgas and do not further influence the Ni/Zn cell.

Research Article
doi.org/10.1002/batt.202500704
Chemistry Europe
European Chemical Societies Publishing

2.1.2. Zinc Electrode

Both the dissolution of the Zn electrode due to Reaction (1) and the precipitation of ZnO due to Reaction (3) as soon as the electrolyte solution is saturated with zincate result in a change of the respective volume fractions, ε^{Zn} and ε^{ZnO}, modeled by balance equations. The latter reaction creates a ZnO shell around the Zn particles which acts as a passivation:[26] If present, the transport of OH^- and $Zn(OH)_4^{2-}$ to and from the zinc surface is hindered (see **Figure 2**). By calculating surface concentrations for these two species, $c^{k,s}$, $k = \{OH^-, Zn(OH)_4^{2-}\}$, this aspect of the zinc electrode enters and influences Reaction (1) and (5). From a Modeling point of view, this is written as a balance between the hindered diffusion through the ZnO shell and the reactions depending on species k happening on the Zn surface,

$$(1-\varepsilon^{ZnO\text{-}L})^{\beta^{ZnO\text{-}L}} D^k \frac{r^{ZnO,o}}{r^{ZnO,i}} \frac{(c^{k,s}-c^k)}{\Delta r} = \sum_r \nu^{kr} j^r \tag{9}$$

where $\varepsilon^{ZnO\text{-}L}$ and $\beta^{ZnO\text{-}L}$ are the volume fraction and the Bruggeman coefficient[46] of the ZnO layer, converting the diffusion coefficient D^k to an effective property. While the two radii $r^{ZnO,i}$ and $r^{ZnO,o}$ correspond to the inner and outer radius of the ZnO shell, respectively, as depicted in Figure 2, their difference Δr is its thickness. The right-hand side of the balance equation contains the sum over all reactions r producing or consuming species k via the reaction rate j^r and the corresponding stoichiometric coefficient ν^{kr}. Furthermore, oxygen recombination (Reaction (7)) takes place at the Zn electrode, which is modeled by a simple chemical reaction equation.

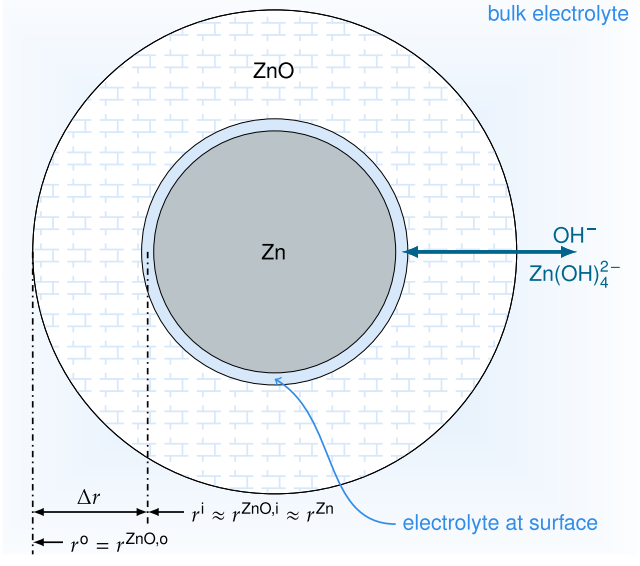

Figure 2. Illustration of a zinc particle with surrounding zinc oxide layer. The layer slows down species transport to the zinc surface, influencing the respective reactions. We assume that the inner radius of the ZnO shell coincides with the outer radius of the Zn particle.

2.1.3. Nickel Electrode

In contrast, at the Ni electrode, an insertion process takes place where protons enter the active material through the electrochemical Reaction (2). From the surface, they diffuse into the particle and are stored by forming $Ni(OH)_2$, see **Figure 3**. Assuming the NiO(OH) particles are perfect spheres, we describe the storage process as a solid diffusion process of the proton concentration c^{H^+},

$$\frac{\partial c^{H^+}}{\partial t} = \frac{1}{r^2}\frac{\partial}{\partial r}\left(D^{H^+} r^2 \frac{\partial c^{H^+}}{\partial r}\right) \tag{10}$$

with r being the radial coordinate in the particle and D^{H^+} being the solid diffusion coefficient of the protons (see Equation (S7), Supporting Information). Since NiO(OH) and $Ni(OH)_2$ show a difference in mass density, the volume fraction of the active material in the Ni electrode would change as in the Zn electrode. As this difference is small, we neglect this effect here.

2.2. Simulation and Setup

The geometry of the simulation setup used in this work follows that of SunErgy's prototype Ni/Zn cell as described in Section S2, Supporting Information. This gives a simulation box for the total cell as it is depicted in **Figure 4**a, which is used in a resolution of $13 \times 21 \times 23$ voxels for simulations where a three dimensionally resolved structure is needed. For all other simulations, a much smaller—and hence computationally less expensive—simulation box is used (see Figure 4b). This thin cut-out of the total cell has a voxel count of $18 \times 3 \times 3$ and may be regarded as a pseudo-1D setup, mainly used for parameter analysis or long-term cycling. In both cases, the solid diffusion in the spherical active material particles in the Ni electrode (cf. Equation (10) and Figure 3) is discretised by five equidistant grid points, while the simulation domains possess a nonequidistant grid to reduce computational costs (see Section S2, Supporting Information). Initial conditions,

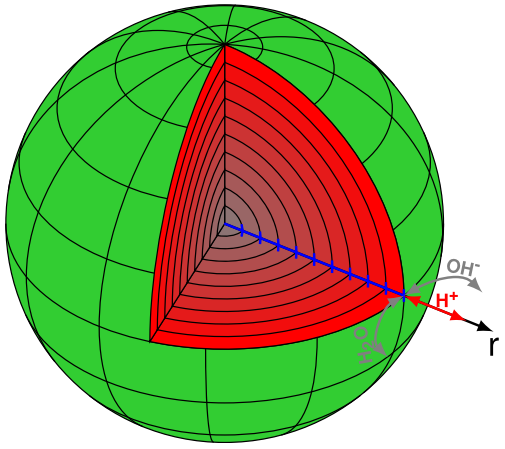

Figure 3. Depiction of a NiO(OH)/$Ni(OH)_2$ particle as a perfect sphere. The protons entering the particle on the surface through Reaction (2) are inserted via a solid diffusion mechanism.

Research Article
doi.org/10.1002/batt.202500704
Chemistry Europe
European Chemical Societies Publishing

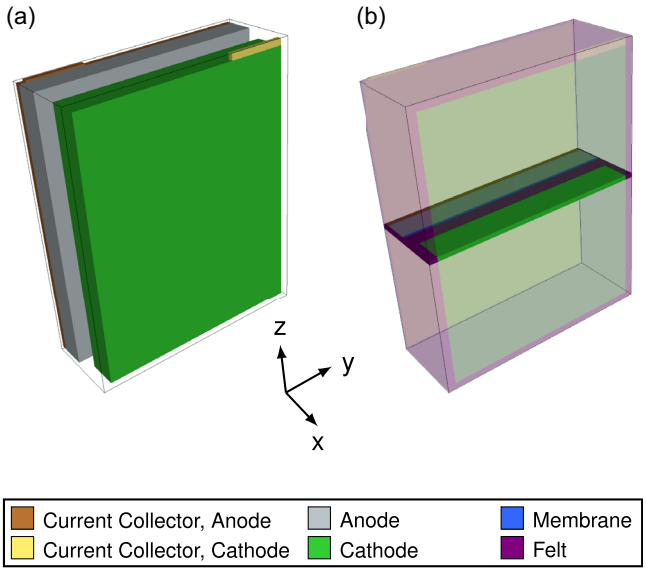

Figure 4. Setup of the simulation boxes. a) Detailed full cell setup, membrane and felt not shown. b) Thin, horizontal slice of the full cell serves as a reduced setup. The x-axis has been scaled by a factor of 10 for a better depiction.

for e.g., the composition of the electrolyte solution or the initial volume ratio of Zn to ZnO, are stated in Section S3 and S4, Supporting Information. The same applies for the general boundary conditions for the applied current or voltage (Section S5, Supporting Information), which are based on the cycling protocols introduced in the section on experimental procedures. The pseudo-1D setup possesses periodicity in the z-direction. As this setup does not include the tab connections, here the current and voltage boundary conditions are applied to the back of the respective current collectors. For this purpose, an artificial and very thin current collector is added to the backside of the Ni electrode (not depicted in Figure 4b, as the actual Ni electrode uses a Ni mesh as a current collector).

We estimated most material constants, such as ion diffusion coefficients or conductivities, from literature as described and given in the Supporting Information, but some parameters lie in a wide range of values due to composition, uncertain additives or other influences, and hence have to be assumed by an educated guess. The various standard reduction potentials $\Delta\phi^{o}$ of the electrochemical reactions, for example, must be adapted to the conditions in the battery cell, but as they follow more specific considerations such as the influence of electrolyte concentration or known additives, they have relatively fixed values discussed in Section S9, Supporting Information. Other parameters with some uncertainty are the reaction rate constants k^{j}, the proton diffusion coefficients $D^{NiO(OH)}/D^{Ni(OH)_2}$, the interaction coefficient γ and the voltage hysteresis $\Delta U^{hyst.}$ of the Ni active material, and the Bruggeman coefficient of the ZnO film around the zinc particles, β^{ZnO-L}. A suitable and meaningful set of values for these parameters is listed in **Table 1**. These parameters were chosen to catch typical characteristics of Ni/Zn cells, as they are depicted in the result section, see **Figure 5**a and 8a. This includes, e.g., the voltage plateau at the end of charge, C-rate dependence of the charge/discharge branch, infliction points of the cell voltage and the CE of the regular cycles. Generally, the reproduction of the regular cycles is prioritized over formation cycles, as they make up the main part of the cycle life.

The model described above and in detail in Section S6–S11, Supporting Information, is implemented in the software package Battery and Electrochemistry Simulation Tool (BEST),[47] using the finite volume method (FVM). The software relies on the software package SAMG[48] to solve the nonlinear system of equations and allows for multiprocess execution using OpenMP. More precisely, we employ the sequential semi-implicit time integration scheme described by Schmitt et al.,[49] which is especially suitable to solve the multicomponent incompressibility constraint arising due to the included electrolyte convection. Schmitt and coworkers implemented this algorithm in BEST and proved its numerical applicability to conversion-type electrochemical cells by analyzing stability (regarding, e.g., problem size, resolution, and time step width) and error.

For the 3D visualization of simulation results the visualization software VisIt[50,51] is used.

2.3. Experimental Procedures

We conduct the following experiments with an 8 Ah Ni/Zn cell prototype (SunErgy).

2.3.1. Cycling Data

Several cycling tests with prototypes of slightly varying parameters, e.g., Zn particle size, have been performed. All prototypes are very similar to the prototype cell described in the Supporting Information.

During initial cycling of a pristine cell, the first three cycles employ a specialized cycling protocol to form and condition the Zn electrode (formation cycles). This deliberate, slow-rate charge/discharge procedure is essential for establishing the initial pore structure of the Zn electrode through the conversion of ZnO to metallic Zn, which exhibits a lower molar volume. Furthermore, this process enhances the conductive network of the metallic

Table 1. Estimated parameters of the electrochemical Ni/Zn cell model.

k^{I} [mol cm^{-2} s^{-1}]	k^{II} [mol cm^{-2} s^{-1}]	k^{IV} [mol cm^{-2} s^{-1}]	k^{V} [mol cm^{-2} s^{-1}]	k^{VI} [s^{-1}]	k^{VII} [s^{-1}]
2.5×10^{-10}	1.0×10^{-7}	2.5×10^{-21}	1.5×10^{-18}	5.0×10^{-3}	3.0×10^{2}
k^{VIII} [s^{-1}]	$D^{NiO(OH)}$ [cm^{2} s^{-1}]	$D^{Ni(OH)_2}$ [cm^{2} s^{-1}]	β^{ZnO-L} [—]	γ [—]	$\Delta U^{hyst.}$ [V]
2.5×10^{-1}	9.5×10^{-11}	1.0×10^{-12}	1.75	−8	0.1325

Research Article
doi.org/10.1002/batt.202500704
Chemistry Europe
European Chemical Societies Publishing

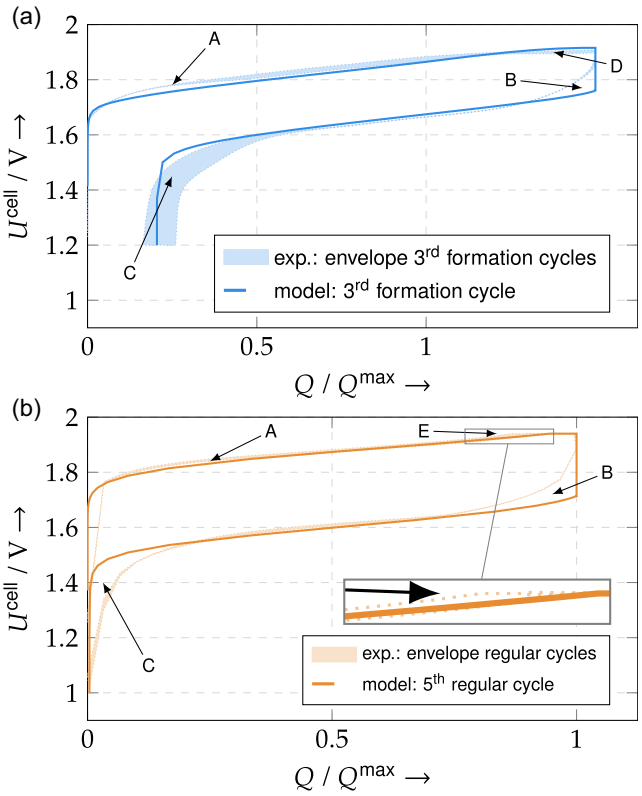

Figure 5. Charge and discharge behavior of the prototype and virtual cell. a) Experimental envelope and simulated curves of the cell voltage over transferred charge of the 3rd formation cycle. b) Experimental envelope and simulated curves of the cell voltage over transferred charge of the 5th regular cycle. Segments of interest in both curves have been marked by letters A to E.

zinc. The formation protocol follows conventional practice: charging at low current density until reaching the characteristic voltage plateau of Ni/Zn cells, followed by a likewise slow discharge. Upon completion of the formation cycles, regular cycling commences, representing the intended operational conditions for this prototype. The standard cycling protocol initiates with charging at a 1C rate until the cell voltage reaches 1.94 V. This is followed by constant voltage (CV) charging maintained until either the projected capacity of $Q^{max} = 8$ Ah has been transferred or the current decreases below $^{C}/_{20}$ as a safety cutoff. The discharge phase proceeds at a 1C rate until the cell voltage falls below 1.0 V.

All cycling data was recorded with a BST8-12 battery analyzer from MTI (5 mA–12 A up to 5 V) following the cycling protocol described above. The data points have been recorded every 120 s. Additions of a few grams of deionized water may have been made every few hundred cycles, if the level of electrolyte decreased because of the water splitting due to Reaction (5) and (6). The combination of cell composition and cycling protocol allows for more than 3800 cycles.

We present the cycling data in the form of envelope curves (see Figure 5a,b), which are, in the case of the formation cycle, a selection of the third formation cycle of different realizations of the prototype. For the regular cycle, the envelope curve comprises a selection of cycles between cycle number 49 and 101 of one realization of the prototype.

2.3.2. μ-XRF Measurements

For the comparison of pristine and end-of-life distribution of elemental zinc, another prototype cell was cycled for ≈1800 cycles. While the formation cycles followed the same procedure as above, the regular cycles had an altered protocol: Constant current (CC) charging was performed at a $^{C}/_{3}$ rate until $Q^{max} = 8$ Ah had been transferred. Discharging happened then again with a 1C rate until the cell voltage dropped below 1.0 V.

A micro X-ray fluorescence (μ-XRF) device (Bruker M4 Tornado) was employed for spatially resolved elemental analysis of the Zn electrode. The μ-XRF images depicting the elemental zinc distribution in the electrode are shown in Figure 10a,b.

3. Results and Discussion

We investigate the cycling behavior of the virtual Ni/Zn cell described in the modeling and setup sections, making direct comparisons with experimental results obtained via methods outlined in the experiment section. The core cycling characteristics of our model are evaluated against experimental data and long-term performance is analyzed to assess model quality and to identify potential improvements for Ni/Zn cells. Results are presented and discussed systematically by topic.

3.1. Charge and Discharge of the Cell

In a first step, we only carry out a few cycles and place an emphasis on the behavior of the model during a single charge/discharge cycle, as well as how it relates to experimental observations.

3.1.1. Cell Voltage During One Cycle

The cycling experiments of the slightly varied prototype cells have been collected in an envelope curve for the third formation cycle and typical regular cycles, see Figure 5. Both cycle types show typical behavior for this cell type. The formation cycle (blue shaded) attempts a full charge, which gives a steadily increasing cell voltage with a slightly convex trend. This increase is slowly diminished and ends in a voltage plateau soon after the projected 8 Ah of transferred charge is surpassed. From here, the cell voltage does not drop abruptly onto the discharge curve but joins it smoothly, before it collapses at the end of discharge. In principle, this behavior is also maintained at the higher C-rates of the regular cycles (orange shaded). Differences show, of course, in the level of the cell voltage, the cycling protocol related voltage plateau and the slightly more convex shape of the charging branch.

These experimental curves have been superposed by the simulation results (solid lines) obtained as described in the simulation section. We observe that for the larger part of the charge and discharge curve, a close agreement between experiments and

simulation is reached. To a certain extent, this is also true for parts where a deviation may be observed, as the same trends may be recognized. For easier identification, these segments, where differences between model and experiment show, have been labeled from A to E.

At the beginning of charge (segment A), experimental cycling curves show a slight rise, more pronounced in the formation cycle. The simulated voltage curve maintains a constant slope. During discharge (segment B), experiments exhibit a small voltage drop followed by a smooth decline forming an arc, equally observed in slow and fast discharging, i.e., formation and regular cycles, respectively. Simulations, however, predict this as a nearly instantaneous drop with a mild arc. Near the end of discharge (segment C), cell voltage declines less abruptly in experiments compared to simulations. Two unique, cycle-specific segments are notable: the formation cycle's end-of-charge plateau (segment D), which the model reproduces imperfectly, and the regular cycle's pre-CV charging stage (segment E), where the cell voltage curve becomes convex (see magnification in Figure 5b), also predicted by simulations but to a lesser extent.

When examining the course of the simulated charge/discharge curve in Figure 5a,b, we see a reasonable reproduction of the respective experiments for both the formation and regular cycle. This underlines the validity of our modeling approach, which shows in several aspects of the curves. Generally, the combination of the models for the conversion-type Zn and insertion-type Ni electrodes is well-suited to depicting the slight but constant increase in cell voltage in the charging phase, as well as the decreasing counterpart during discharging. The kinetics of Reaction (1), (2), and (6) and their overpotentials together with a reasonably-scaled voltage offset used in our model (cf. Section S9, Supporting Information) describe accurately enough the height of the voltage drop when switching from charging to discharging, and in conjunction with the solid diffusion proton transport into the Ni active material, the cell voltage breakdown at the endof-discharge is sufficiently matched. Besides this, further issues are covered, which are most prominently the end-of-charge voltage plateau induced by the OER (formation cycle, blue), suppressing the extraction of protons from the active material and keeping the cell voltage at a level comparable to the experimental findings, and the behavior when switching from CC to CV charging in the regular cycle (orange). There, the cell voltage development is close to the experiments, which shows especially in the continued charging operation after switching to CV, indicating a suitable modeling of the continued proton extraction from the Ni active material. Since all of this also happens sufficiently accurately at the different C-rates involved when charging and discharging in formation and regular cycles, the model is suitable for realistic simulations of a Ni/Zn cell.

However, the simulations are not identical to the experiments, as shown in points A to E marked in Figure 5a,b. These deviations are mostly rooted in the compactness of the model, which leaves out details, e.g., the influence of additives as $Ca(OH)_2$ in the Zn electrode (see Table S3, Supporting Information), or uses simplified approaches, e.g., for multistep Reaction (1), (5), and (6). The latter certainly affects the rate dependence of the model, and more detailed descriptions would be possible, e.g., to capture the complexity of the OER.[52] Although these deviations are considered minor in the context of the overall functioning of the model, we may still obtain a better understanding of the model and relevant processes in the Ni/Zn cell by assessing them.

The slight voltage bump in *segment A*, which wears off in the course of charging, indicates an initial, temporary transport hindrance. This may be linked to the permeability of the ZnO layer or the proton diffusion in the Ni active material. Both have their most unfavorable configuration at this stage, i.e., maximum layer thickness and the highest amount of diffusion-inhibiting $Ni(OH)_2$. Indeed a bump may be induced by e.g., varying the Bruggeman coefficient $\beta^{ZnO\text{-}L}$ or the diffusion coefficient $D^{Ni(OH)_2}$. However, these effects should scale with the C-rate, but the bump seems to be lower in the regular (1C) than in the formation cycle ($^{C}/_{10}$). A possible explanation is the shift of the state of charge (SOC) window with higher C-rates (cf. Figure 8c), as discussed in the next section. Through this shift at 1C, the lower SOC regions connected with the previously described transport hindrances are avoided naturally. Furthermore, other influences such as the role of $Ca(OH)_2$ or non-wetted active surfaces due to the convection of the electrolyte solution may play an additional role, and lastly, as the bump is only pronounced in the formation cycles, it may simply be connected to the Zn electrode formation process, in which large parts of the initial, transport-hindering ZnO is converted bit by bit to Zn.

In *segment B*, the behavior of the cell voltage consists of two parts: a small instantaneous drop followed by a gradual decline. While the former may be attributed to the change in reaction overpotentials from charge to discharge operation, the latter indicates an uncovered time- or charge-dependent process. This process affects only that part of the voltage difference between charge and discharge branches, which is commonly identified as the hysteresis of the β-NiO(OH)/β-$Ni(OH)_2$ electrode.[32,53–55] The true physical reason for this hysteresis is still unknown, but a reordering or transformation process in the Ni active particles would explain the slow drop in voltage. More recent investigations[56,57] indicate the formation of a kinetically-favored, metastable TP2 phase upon charge, while during discharge a thermodynamically-favored pathway may be used, leading to a loss of energy and thus a voltage drop. But due to the yet unclear origin, we model this hysteresis by a simple voltage offset between discharge and charge branch (cf. Section S9, Supporting Information), which explains the deviation between simulation and experiment.

In *segment C*, the voltage collapse at the end of discharge happens, which is accurately predicted by position but not so much in shape. During discharging, Reaction (2) inserts protons into the outer shell of the Ni particles, which diffuse into the active material. This diffusion gradually slows down as more protons are inserted, and at one point, protons are inserted into this outer shell faster than they can be transported deeper into the particle. When the outer shell reaches its limit, the voltage

Research Article
doi.org/10.1002/batt.202500704
Chemistry Europe
European Chemical Societies Publishing

collapses. In addition, the concentration overpotential of Reaction (2) influences the rough voltage curve at this point. Thus, possible remedies could involve the introduction of either Ni particles of different size to smear out the voltage drop or surface concentrations at these particles to have a stronger influence of the concentration overpotential. Neither of them is used here for the sake of model simplicity. A different possibility would involve varying the relevant reaction constant k^{II}, which may smooth this segment as discussed in Section S12.2, Supporting Information. Due to its strong influence on an overall consistent cell behavior, this possibility was ruled out.

The behaviors observed in segments D and E represent distinct electrochemical processes that are interlinked. We analyze each segment separately before examining its mutual influences.

At *segment D*, during the formation cycle, a voltage plateau is reached due to a dominating OER at the end of charge. The O_2 formation is in competition with the proton extraction reaction, which shifts into a less favorable overpotential region when most protons have been extracted from the active material. The slightly underestimated OER resulting in a higher voltage plateau compared to the experimental curves could easily be corrected by modifying its reaction constant k^{V}, which also controls the onset of the very same plateau.

Segment E, see the magnification in Figure 5b, points out the region before the cycling protocol switches from CC to CV charging, which happens upon reaching a cell voltage of $U^{cell} = 1.94$ V. Due to its convex voltage curve, the experiments attain this limit earlier than the simulation, which remains relatively flat. This onset of convexity indicates that, similar to what has been discussed for segment C, the Ni particles' outer shells are nearly depleted of protons through the extraction Reaction (2), resulting in a rise of the SOC-dependent OCP of the very same reaction. At the same time, the OER seems not to be strong enough yet to suppress this convexity, which is beneficial for the CE of the cell. To bring the simulation closer to the experimental observation, the solid diffusion coefficients $D^{NiO(OH)}$ and $D^{Ni(OH)_2}$ have to be reduced, so that the extraction limit is reached earlier and a convexity is established. However, this may also influence the overall steepness of the charging branch.

After the mechanisms of the two segments have been considered individually, their interaction and its consequence for the Ni/Zn cell are discussed. The use of a stronger OER to adjust the voltage plateau (segment D) inevitably shifts its onset, which may already flatten the voltage curve in segment E, restraining the desired convex behavior. This results in a reduced CE. Conversely, changing the solid diffusion constants to tune the behavior in segment E increases the cell voltage earlier on, which may translate to overpotentials at the Ni electrode that favor the OER too soon, leading again to a lower CE. This may be counteracted by attenuating the OER, but with the negative effect of a voltage plateau in segment D, which deviates from the experimental observation. The approximation of these two processes in our model is hence a compromise, where both segments have a small deviation from the experimental data, while the CE reaches realistic values as discussed in the next section.

A secondary consequence of this interplay is the placement of the cycled 8 Ah capacity window within the total SOC range during regular cycling (discussed in the following section, see Figure 8c). The faster the solid diffusion is assumed in our model, the lower SOCs are possible at the end of discharge, which pushes the cycled capacity window away from the beginning of the OER. However, for realistic values of the solid diffusion coefficients, the upper end of this window is at the onset of the OER, which agrees with experimental observations and thus speaks in favor of a good approximation by the model. As a result, this further narrows down the scope of the involved parameters k^{V}, $D^{NiO(OH)}$, and $D^{Ni(OH)_2}$. More profound approaches for a better approximation of the experimental cell voltage curve may therefore be, as before, a more complex modeling in the form of, e.g., a multistep reaction for the OER or the use of a particle size distribution to disperse the behavior of the solid diffusion.

3.1.2. Parameter Influence

In the previous section, we have seen that only a certain balance between all processes makes it possible to approximate the experimental cell voltage curves. This is particularly evident in the delicate interplay of effects in segments D and E, and raises the question in which manner the parameters listed in Table 1 affect the cell's behavior. To shed more light on this influence, the reaction rate constants of the two main Reaction (1) and (2) and the prominent O_2 formation Reaction (6) are being varied here. The reference scenario is the previously shown cycling curve of the formation cycle.

Figure 6a shows the effect of slowing down Reaction (1) in two steps. The respective charge and discharge branches are shifted almost parallelly from the reference, explainable by the conversion-type reaction in conjunction with the negligible influence of the HER (Reaction (5)), giving a higher overpotential at the Zn electrode uniformly throughout the cycle. Similarly, in Figure 6b, the proton insertion Reaction (2) at the Ni electrode is diminished. Here, the strong competition with the OER

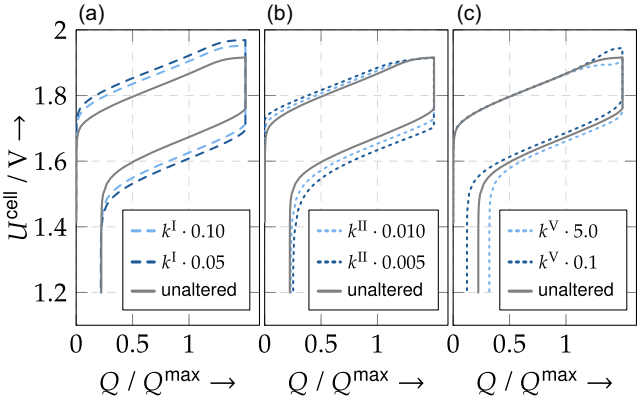

Figure 6. Sensitivity of the cell voltage curve to parameter variations during the third formation cycle: a) Reaction rate of the zinc dissolution k^{I}, b) reaction rate of the proton insertion k^{II}, and c) OER rate k^{V}. The reference simulation with standard parameters is given in dark gray.

(Reaction (6)) leads to the fact that the charge branches converge toward higher SOCs with the reference simulation. The reason is that at low SOCs the additionally necessary overpotential at the Ni electrode is provided by Reaction (2) while then successively the OER is favored with its unaltered reaction rate. When discharging, the OER does not play a role, and hence the discharge branch is again mostly shifted parallelly. Except close to the voltage drop at the end of discharge, when the manipulated proton insertion rate plays on the proton diffusion in the Ni active material. The result of varying the OER rate is shown in Figure 6c. A higher rate means an earlier onset of the end-of-charge voltage plateau and hence an extended period of O_2 production, because the OER becomes favorable over the proton extraction earlier on. Subsequently, due to the lesser number of protons extracted during charge, the discharge capacity is reduced and the final voltage drop happens earlier. When lowering the OER rate, the effects are reversed: The OER takes over later during the charging period, meaning at a more elevated cell voltage and for a shorter period, giving a higher discharge capacity.

Visibly, the three as examples chosen reaction rates have a diverse influence on cell voltage of the Ni/Zn battery, and in the case of the competing proton insertion Reaction (2) and O_2 formation Reaction (6), on the discharge capacity. Measures that tip the balance in favor of Reaction (2), e.g., through additives suppressing Reaction (6), would directly improve the CE.

Further sensitivity studies may be found in Section S12.2, Supporting Information.

3.1.3. Convection During One Cycle

When examining the cycling behavior of the virtual cell, another important detail is the convection of the electrolyte solution it contains. Its observed movement during charge has been schematically illustrated in **Figure 7**. We see that liquid moves out of the Zn electrode (A) toward the membrane (M), felt (F), and ultimately the Ni electrode (C) and the regions next to it. This happens strongly through central pathways, but also involves movement through the outer parts of the cell components. When discharging, this process is reversed, and liquid is sucked back into the Zn electrode.

The model-based convection behavior shown in Figure 7 suggests a counter-intuitive flow of electrolyte solution during cycling. By just reasoning on the basis of the Zn/ZnO conversion, the charge operation should lead to a significantly enlarged pore space due to the 40% smaller molar volume of Zn, sucking the electrolyte solution into the Zn electrode as, e.g., assumed by Choi and coworkers.[21,35] But when accounting for all species consumed and created in Reaction (1) and (3), based on our parameterization, the volume of the electrolyte solution expands more than the pore space (approximately in a ratio of 4 to 1). This trend also applies to the single steps of the overall dissolution-precipitation process. Hence, a counter-intuitive convection scheme is found, and in its consistency along the whole reaction chain, it may indicate a prominent role in the cell. This reasoning has already been made by Einerhand et al.[58,59] on an experimental basis, and has been described under the term *density gradient model* in their work. They note that the convection pattern plays an important role in zincate redistribution and hence is partly responsible for the zinc shape change, and also rule out other ideas as the (sole) influence of the membrane or concentration cells given by other authors.[60–62] Additionally, as supporting evidence, our cycling experiments show a moderately increasing electrolyte solution level during discharge.

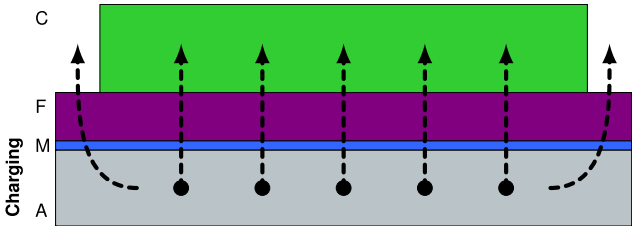

Figure 7. Schematic movement of the electrolyte solution in the virtual cell (dashed arrow) during charge. The liquid is forced out of the Zn electrode. When discharging, the direction is reversed. The different regions mark the Zn electrode/anode (A), the membrane (M), the felt (F) and the Ni electrode/cathode (C).

For a more precise analysis, however, other influences such as the slight volume change of the Ni electrode when H^+ insertion/extraction is happening and the headspace volume should be taken into account.

3.2. Long-Term Cycling of the Cell

For this section, the previously presented simulation is continued until the virtual cell starts to fail. This happens after ≈269 regular cycles when the capacity starts to decline, see **Figure 8**. The corresponding evolution of the internal configuration of the battery cell is shown in **Figure 9**. Furthermore, a 3D simulation is done for an evaluation of the zinc shape change process.

3.2.1. General Cell Behavior

In a first step, we compare the results of our simulation to the characteristic quantities of the prototype cell, namely the cell voltage U^{cell} and the CE φ^C. This is accompanied by a glimpse of the cycled SOC window.

In Figure 8a, we see cell voltage curves during regular charge/discharge cycles over transferred charge normalized to the cell's 8 Ah capacity. In the background, as before, we see the envelope of several cycles of the experiment, which lie in the range of cycle numbers 49–101 (cf. section on experimental procedures). On top of this, the simulation's cell voltage curves are drawn, from dark blue to dark red in ascending cycle numbers. Since most of the visible colors are dark red, this means that the cell voltage curve does not change a lot during the cycling simulation, except at the very end of cycle life, when the point at which the cycling protocol switches from CC to CV charging shifts to the left and later the charging finishes prematurely.

Figure 8b shows the CE of our simulations (orange) and of the experiments performed (blue) over time during cycling. The two

Research Article
doi.org/10.1002/batt.202500704
Chemistry Europe
European Chemical Societies Publishing

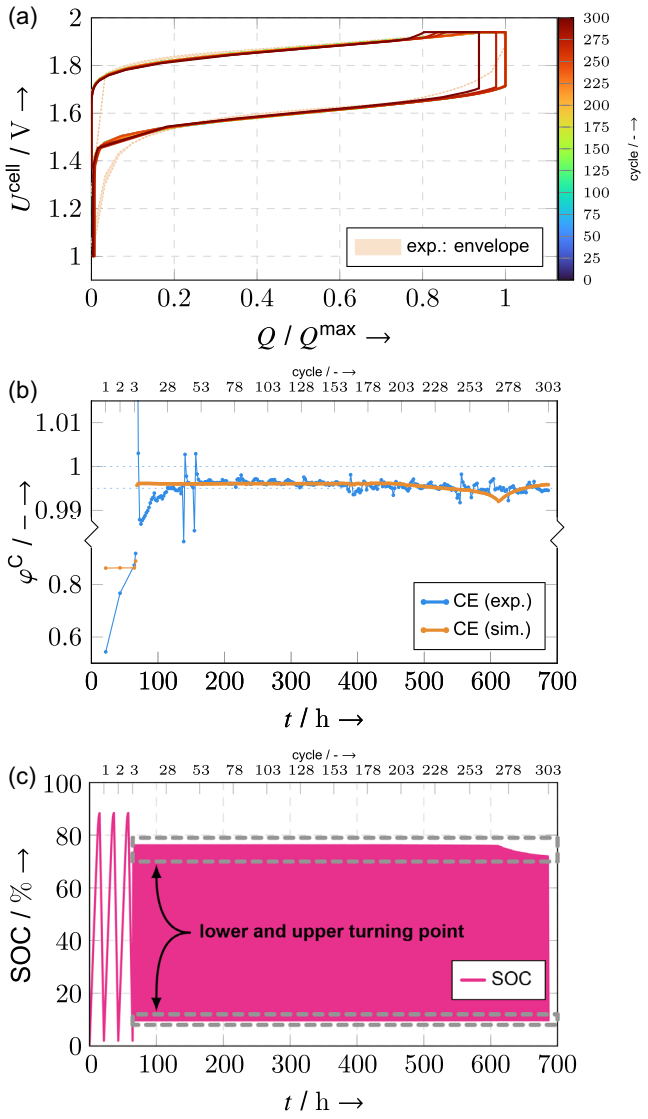

Figure 8. Results and comparison of long-term cycling. a) Cell voltage over transferred charge: regular cycles compared to experimental envelope with simulation failure starting at regular cycle 269 (equals total cycle 272). b) The development of the Coulombic efficiency (CE) and c) of the SOC over time. The CE is always depicted at the end of a charge/discharge cycle and compared to the CE of a cycling experiment. The CE *y*-axis' upper part is differently scaled to better show details around $\varphi^C = 1$.

distinguishable time segments are the formation cycles 1–3 and the subsequent regular cycles until the start of cell failure. During the formation cycles, the efficiency in the experiments increases from ≈0.55 to 0.87, while the simulation shows a steady value of 0.85. When switching to regular cycles, the overall behavior of experiment and simulation is similar: The CE stabilizes in a range between 0.995 and close to 1.0 (indicated by the two blue dotted lines). The simulation result fluctuates in a barely visible, much narrower range. Differences are noticeable in two points. First, at the beginning of the regular cycles, the experiments show an initial spike followed by a short dip, whereas the simulation directly attains stable values. Second, at the end of the cycle life of the virtual cell, its CE slowly drops until a visible minimum at regular cycle 269 before rising again afterward. In contrast, at this point, the prototype cell is still far from cell failure and shows, therefore, no unusual features.

The last panel, Figure 8c, depicts the development of the simulated cell's SOC over time. Again, the two segments of formation and regular cycles are clearly separable. The SOC ranges in the formation cycles from nearly 0% to ≈90% and in the regular cycles in a window between ≈10% and 76%. After regular cycle 269, the SOC and hence the available capacity starts to drop visibly. Generally, we see that the lower and upper turning points of the SOC remain very stable throughout cycling.

The battery model also shows in the long-term cycling simulation a behavior which approximates the experiments closely. Like these, it predicts stable cycles (Figure 8a) characterized by high CE (Figure 8b) and a constant SOC window (Figure 8c) throughout cycle life. Even small but barely visible fluctuations in both CE and SOC are reproduced.

The two major deviations from the experimental CE are readily explained. During formation and initial regular cycles, the experimental data show behavior not captured by the model, as Zn electrode formation processes are not covered. However, the model successfully reproduces the third formation cycle, which was used for parameter adjustment. Furthermore, the initial differences in the regular cycles are mostly due to the experiments using two other cycling protocols before switching to the one used by the simulation. At end-of-life, the virtual battery exhibits a complex behavior. The internal configuration has changed to such an extent, i.e., zincate shortage acting on concentration overpotentials (see next section), that the voltage limit to switch from CC to CV charging is reached earlier on (see Figure 8a), and hence an extended period of high voltage promotes oxygen formation, resulting in a phase of steadily declining CE. At the minimum of CE, regular cycle 269, the CV period has developed a length which lets the charging current drop below the limit defined in the cycling protocol (cf. the experimental procedures section) before reaching 8 Ah of transferred charge. In consequence, the SOC window cannot be maintained—the dischargeable capacity starts to diminish. Due to this now dominant limit for end-of-charge, the CV period shortens again, which leads to less O_2 formation and thus the CE rises again while the SOC window continues to shrink. At the same time, the again increasing CE starts to get limited by the HER, which slowly gains weight due to the aforementioned changes in internal configuration. Therefore, the already mentioned regular cycle 269 poses here as an indicator of maximum cycle life. This is little compared to the more than 3800 cycles reported for the experiment, but not unusual as our model and its parameterization do not cover all aspects of the prototype cell. For example, the 8 Ah prototype cells mainly failed due to cracking and subsequent loss of active material in the Ni electrode. This effect, mainly driven by the repetitive volume changes of the $NiO(OH)/Ni(OH)_2$ electrode when charging and discharging, is not covered by our model, as well as aspects of different additives such as $Ca(OH)_2$ in the electrodes and the electrolyte. Naturally, this could mean a progressively divergent behavior of the model with each cycle compared to the experiment. This is not inherently negative, as it may

Research Article
doi.org/10.1002/batt.202500704
Chemistry Europe
European Chemical Societies Publishing

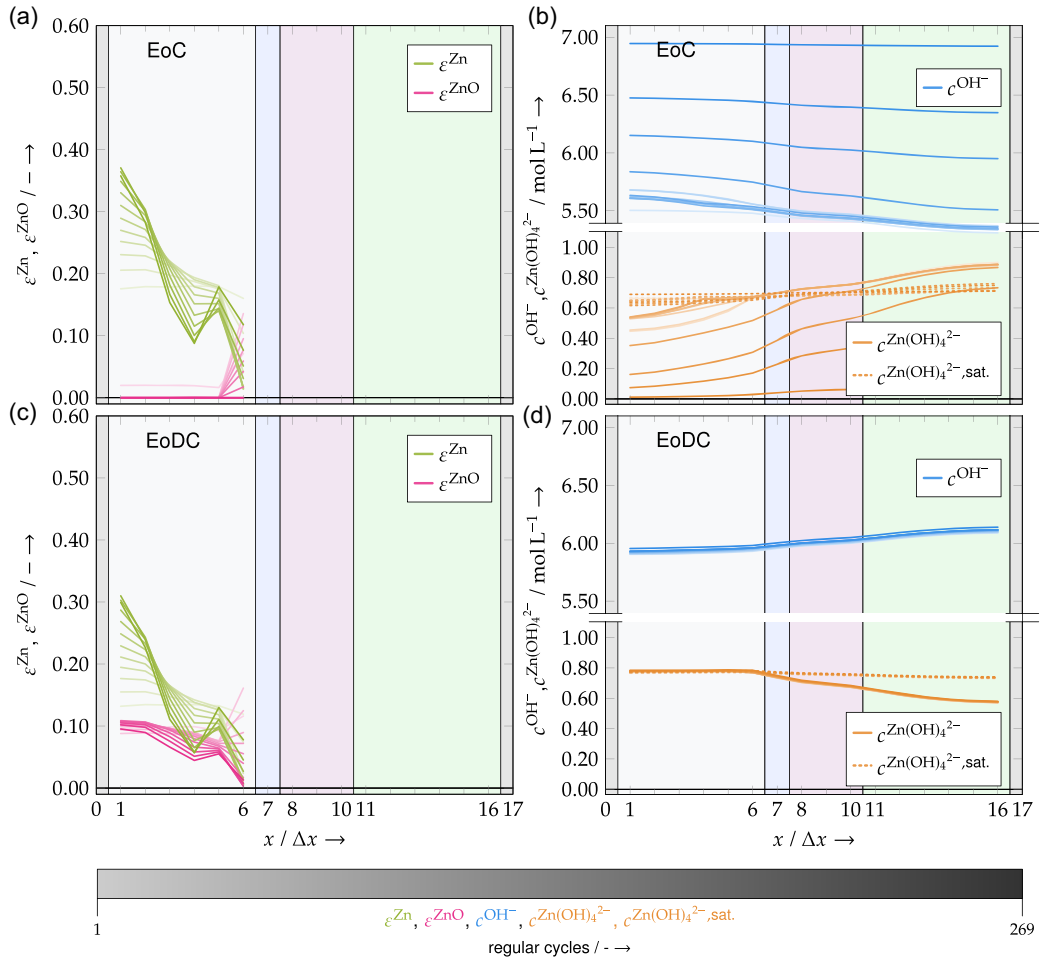

Figure 9. Evolution of volume fractions and concentrations along the x-direction of the cell. Regular cycles 1, 25, 50, 75, 100, 125, 150, 175, 200, 225, 250, and 269 are depicted with lines of increasing color intensity. a,c) Show the volume fractions of Zn and ZnO at the end of charge and end of discharge, respectively. Similarly, b,d) show the concentration profiles of OH^-, $Zn(OH)_4^{2-}$ and its saturation concentration at the end of charge and end of discharge, respectively. The background colors indicate the compartment of the cell according to Figure 4.

assist in identifying important processes for cycle stability, and hence in refining the general model. Furthermore, while long-term predictions may not be accurately close to the prototype cell's behavior, the model still allows to learn about the processes modeled, which may be studied in their pure functioning without the interference of other failure processes.

Nevertheless, the virtual cell continues to cycle until regular cycle 395, in which around 85% of the initially utilized capacity is still accessed and the cell fails due to continued zinc redistribution and follow-up transport restrictions.

3.2.2. Internal Configuration

Beyond this rather external characterization of the cell behavior, the simulation enables us as well to examine the internal dynamics that drive the observed behavior. For this purpose, we analyze the evolution of the volume fractions of Zn and ZnO and the concentration profiles of OH^- and $Zn(OH)_4^{2-}$, depicted for the end of charge (see Figure 9a,b) and the end of discharge (see Figure 9c,d), respectively.

Initially, Zn and ZnO volume fractions (Figure 9a) show nearly equal distribution at the end of charge, with some variation near the membrane. However, as cycling progresses, Zn increasingly accumulates toward the current collector while ZnO quickly depletes throughout the electrode, last disappearing near the membrane. In advanced cycle stages, ZnO is completely consumed across the entire electrode at the end of charge, while Zn develops a small peak due to spatially different growth rates.

The concentrations in Figure 9b show a certain stability up to the first 150 to 175 regular cycles, with the profiles of both, c^{OH^-} and $c^{Zn(OH)_4^{2-}}$, remaining in a narrow range. For the zincate concentration, for some time a relatively flat profile is observed from the membrane halfway into the electrode. Later, the profiles start to deviate from this behavior, with c^{OH^-} increasing and $c^{Zn(OH)_4^{2-}}$ decreasing substantially. Near end-of-life, the zincate concentration drops to near zero throughout the cell, while its saturation concentration remains relatively stable. Generally, the spatial distribution shows GOH^- decreasing from negative to positive electrode, with $Zn(OH)_4^{2-}$ exhibiting the inverse behavior, including that of its saturation concentration.

At the end of discharge, the trend for and the shape of the volume fraction of Zn is similar to that at the end of charge but with lower absolute values due to zinc dissolution during discharge (Figure 9c). For ZnO, the volume fraction has the tendency to be higher close to the membrane at the beginning, but progressively shifts toward the current collector over cycling.

In contrast to the changes observed at the end of charge, concentration profiles at the end of discharge (Figure 9d) remain relatively stable with increasing cycle number. For OH^-, the profile increases constantly from the Zn to the Ni electrode, while zincate decreases between these two electrodes. Its saturation concentration shows only a minimal decline.

The general observations show once more that the model captures the essence of the functioning of the battery. When, e.g., bringing a charging process to mind, roughly corresponding to the differences of volume fractions and concentrations between EoC and EoDC in Figure 9, the following consistent picture is drawn: Zn increases in the anode through Reaction (1), consuming $Zn(OH)_4^{2-}$. This causes the zincate concentration in the Zn electrode to drop below its saturation limit, which results in the dissolution of ZnO via Reaction (3). In combination, these two reactions release two hydroxide ions reflecting in an increase of OH^- concentration in this compartment. At the other electrode, extraction of protons from the nickel active material via Reaction (2) consumes OH^-, explaining the drop of its concentration in the cathode.

Furthermore, the observations reveal critical insights into the cell functioning and failure mechanism. Despite the virtual cell cycling in a relatively stable manner until the very end (cf. Figure 8a), examining the changes in ZnO volume fraction (Figure 9a) and $Zn(OH)_4^{2-}$ concentration (Figure 9b) shows that progressive depletion of ZnO and subsequent zincate shortage in the electrolyte solution causes an increased concentration overpotential for Reaction (1). This leads to the previously observed earlier onset of the 1.94 V plateau, ultimately initiating cell death.

Before cell death, at advanced cycling stages, redistribution of Zn and ZnO fuels this problem additionally. The accumulation of these toward the current collector, which is in agreement to experiments,[63] reduces pore space and progressively restricts zincate supply toward the rear parts of the negative electrode during charging, amplifying the aforementioned mass transport limitations. It has been found that the observed bump in the Zn volume fraction depends on the cycling conditions, whereby a longer charging period, i.e., a higher transferred charge, prevents formation. Furthermore, lowering $\beta^{ZnO\text{-}L}$ and hence reducing the transport hindrance of the ZnO layer has similar effects.

This redistribution of Zn and ZnO is already initiated at the beginning of cycling, as shown by the initial dip and peak of these two volume fractions at the membrane. Due to transport of zincate to the negative electrode during charging, the $Zn(OH)_4^{2-}$ concentration is the highest close to the membrane, see Figure 9b. This has two effects: First, ZnO is not dissolved as strongly as in the rest of the anode because the zincate concentration does not drop too much below its saturation concentration. This has the side effect that the ZnO layer around the Zn particles stays thicker in this region, restricting the transport of $Zn(OH)_4^{2-}$ and OH^- to the particle surfaces. Second, together with the higher bulk zincate concentration, this slows down the zinc deposition during charging close to the membrane. This inhomogeneity and reciprocation of local reaction rates and volume fractions is then perpetuated spatially and temporally.

The diminishing zincate concentration in later stages also explains the previously observed changes in CE and SOC near end-of-life. As zincate depletes, hydroxide concentration rises correspondingly, creating two competing effects. First, this concentration shift alters the overpotentials for both insertion and OER, favoring the former due to its single-step mechanism that consumes only one hydroxide molecule compared to the more complex oxygen evolution pathway. Consequently, the insertion reaction becomes increasingly dominant over oxygen evolution. Second, low zincate concentration triggers the aforementioned earlier onset of the CV charging phase through increasing the concentration overpotential of Reaction (1), extending the period of accelerated O_2 production. The latter effect overcompensates the former, explaining the intermediate CE decline observed in Figure 8b. With continued cycling, the CV charging phase reaches an extent such that at its end the current drops below the secondary limit defined in the cycling protocol, terminating the charging phase before having transferred 8 Ah. This creates the local minimum of CE visible toward the end of cycling. As zincate scarcity increases, the onset of the CV phase occurs progressively earlier, which causes the charge termination to depart from the desired 8 Ah. This reduces dischargeable capacity, as reflected in SOC development. However, a lower SOC also weakens the OER, which in turn improves CE again.

The failure mode observed in the simulation demonstrates that near-perfect cycling between Zn deposition during charge and ZnO precipitation during discharge is crucial for successful Ni/Zn cell operation. This delicate Zn/ZnO balance requires almost perfect back-and-forth conversion, which is primarily achieved and reflected through a high CE. High efficiency enables the cell to maintain Zn and ZnO equilibrium by keeping oxygen evolution at minimal levels. Additionally, ZnO recovery in each cycle is partially supported by the recombination of Zn and dissolved $O_{2(aq)}$ as described by Reaction (7). Together, these mechanisms contribute to cycling stability, but their imperfection, also with regard to redistribution, represents a primary pathway to cell failure.

3.2.3. Zinc Redistribution

The analysis of Figure 9 revealed that Zn and ZnO redistribution may impact cell behavior. To comprehensively examine this phenomenon, we established a 3D battery simulation following the setup in Figure 4a.

The simulation parameters remain identical to those in the previous study, but to account for the increased Zn electrode and its surplus compared to the Ni electrode in the 3D geometry,

Research Article
doi.org/10.1002/batt.202500704
Chemistry Europe
European Chemical Societies Publishing

the specific surface area for the HER is reduced by a factor of 0.3. This adjustment ensures comparable H_2 production to previous pseudo-1D simulations. To allow for better comparison, we applied the same cycling protocol as for the μ-XRF experiments.

The computational expense of 3D simulations, driven by numerous variables and nonlinearities, limited our study to a small number of cycles. We avoided 2D domains to maintain realistic convection behavior, though this prevented long-term studies where shape change may become more pronounced and could strongly influence battery performance.

Both experiment and simulation, depict the elemental Zn distribution in wt%, i.e., the zinc in metallic Zn and ZnO. In case of the experiment, this is based on μ-XRF measurements (for details see the experimental procedures), while the simulation calculates the weight percentage assuming the electrode composition from Table S3, Supporting Information, which may deviate slightly from actual electrode values.

Figure 10a,b present μ-XRF measurements of a prototype zinc electrode before and after extensive cycling (1800 cycles). Initially, elemental zinc distributes nearly homogeneously throughout the electrode. During cycling, zinc progressively migrates from the outer edges and corners toward the electrode center.

The simulation results (Figure 10c–i) show elemental Zn distribution viewed from the electrode backside. We narrowed the color band range around initial composition values to visualize subtle distribution changes at this early cycling stage, while experimental images display the full range. The colormap differs slightly but maintains the same red-to-blue gradient.

Starting from homogeneous distribution in the first formation cycle (Figure 10c), elemental Zn accumulates in the center region during both formation and regular cycles. This accumulation persists throughout individual cycles, as evident when comparing end-of-charge and end-of-discharge states. Detailed analysis (see Figure S10, Supporting Information) reveals that metallic Zn predominantly occupies the center region while ZnO appears off-center. The simulation shows distinct behavior along the electrode edge, where elemental Zn accumulation occurs during the simulation time span—a pattern not observed in experiments.

This elemental Zn redistribution in experiment and simulation represents the well-known shape change phenomenon in Zn electrodes[5,8–11]—a 3D effect. Already after ten regular cycles, the simulation demonstrates lower elemental Zn content at electrode edges compared to the center in both fully charged and discharged states. While this difference amounts to only a few percentage points by weight at this early cycling stage, the model successfully captures realistic Zn redistribution behavior.

The increase of elemental Zn along electrode edges differs from μ-XRF observations and represents a distinct phenomenon from classical shape change. This occurs because electrode edges experience heterogeneous electrode and electrolyte potentials, leading to different reaction rates and accelerated dendrite growth. To mitigate this behavior, Zn electrodes are typically oversized in y- and z-directions compared to Ni electrodes,[8] moving undesired effects away from directly facing electrode

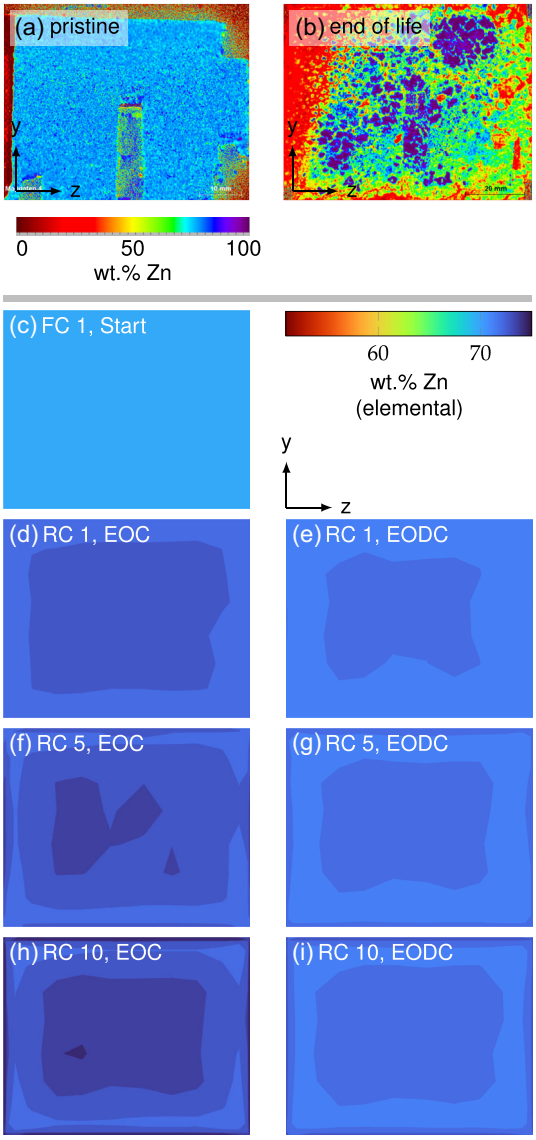

Figure 10. Zn distribution in prototype and virtual cell. a,b) Show μ-XRF scans of the Zn electrode before and after long-term cycling. An accumulation of zinc in the center of the electrode is visible, while the outer regions deplete. c–i) Show the backside of the virtual Zn electrode at end of charge (EOC) and end of discharge (EODC) at different cycles. Color scheme is adapted to the experimental one, but with a narrower band to visualize differences at this early stage of cycling.

regions and creating more homogeneous potentials with evenly distributed dissolution-precipitation patterns, thus helping to extend cycle life.

Our model successfully demonstrates shape change capabilities in these relevant central regions. Comparison with experimental results (≈1800 cycles), Figure 10b and literature[8,58,59,64] shows qualitatively similar trends. The uneven densification and agglomeration of elemental Zn primarily at the electrode center represents a well-established phenomenon. While 10 regular cycles provide limited quantitative insight, subtle color variations indicate early stage elemental zinc unevenness that likely serves as the precursor to more pronounced zinc shape change observed in long-term cycling.

Research Article
doi.org/10.1002/batt.202500704
Chemistry Europe
European Chemical Societies Publishing

3.3. Optimization

Previous sections and analysis of parameter influences in Figure S8, Supporting Information, reveal that the reaction rate constants of the main reactions and OER, amongst others, significantly impact the virtual battery cell's behavior. This may translate similarly to (physical) Ni/Zn cells, offering room for improvements. Previous sections have demonstrated that the competition between OER and the insertion reaction critically determines cell efficiency, directly affecting the Zn/ZnO balance, which is crucial for short to medium-term cycle stability—before longer-term effects like zinc shape change become predominant. Thus, we will focus here on ways to minimize the OER influence and hence optimize Zn/ZnO balance to improve the efficiency and therefore the cycle life. A second objective is to find out whether these efficiency gains can also be translated into higher capacity utilization.

The most straightforward method would be to delay the onset and reduce the strength of the OER by lowering the reaction rate constant (cf. Figure S8b, Supporting Information), which could correspond to the use of additives, for example. Another possibility shows, when plotting the ratio of the volume-averaged side reaction rate to main reaction rate for the two electrodes over the volume-averaged SOC while charging, the operation where the OER occurs. In **Figure 11**a we have simulated this for several C-rates. The ratios for the Zn electrode are given in solid lines, while dashed lines represent those for the Ni electrode.

Two observations may be made: First, the ratio IV/I, i.e., HER to zinc deposition, is largely invariant to the SOC. Only larger C-rates start to disturb this image. The ratio V/II, i.e., OER to proton extraction, however, is strongly dependent on the SOC with the OER constantly gaining weight when charging. Second, moderate C-rates seem to lower the ratio V/II somewhat when compared to low or high C-rates, which is in principle also true for the ratio IV/I, but to a lesser extent.

The first observation may be explained by the fact that the overpotentials of Reaction (1) and (5) are relatively constant, only influenced by concentration changes, which especially show at higher C-rates and SOCs. In contrast, the overpotential of the extraction Reaction (2) strongly depends on the SOC via the OCP curve (see Equation (S21), Supporting Information). This dependence explains why the OER becomes dominant at higher SOC values, shifting the ratio of the two reaction rates in favor of the OER. The second observation, however, is not that trivial, and comprises two aspects in the case of the Ni electrode. For all reactions, the overpotentials depend on local species concentrations, which change proportionally to the applied charging current. Due to the multistep and multielectron nature of most reactions involved, concentration changes affect the overpotentials and Butler–Volmer equations differently. At intermediate C-rates, a favorable combination of concentration profiles, electrode potentials and electrolyte potentials emerges, benefiting the main reactions. At the Ni electrode, the extraction reaction further influences this behavior through the SOC-dependent OCP, which is determined by the local SOC in the active material particle's outer shell. When C-rates are high, this outer shell depletes more rapidly, making proton extraction less favorable compared to OER. Simultaneously, protons in the particle core cannot escape due to solid diffusion being slower than the reaction rate, causing a low SOC. At intermediate C-rates, however, the extraction rate and solid diffusion remain sufficiently balanced, allowing the system to reach high SOC values before OER becomes the dominant process.

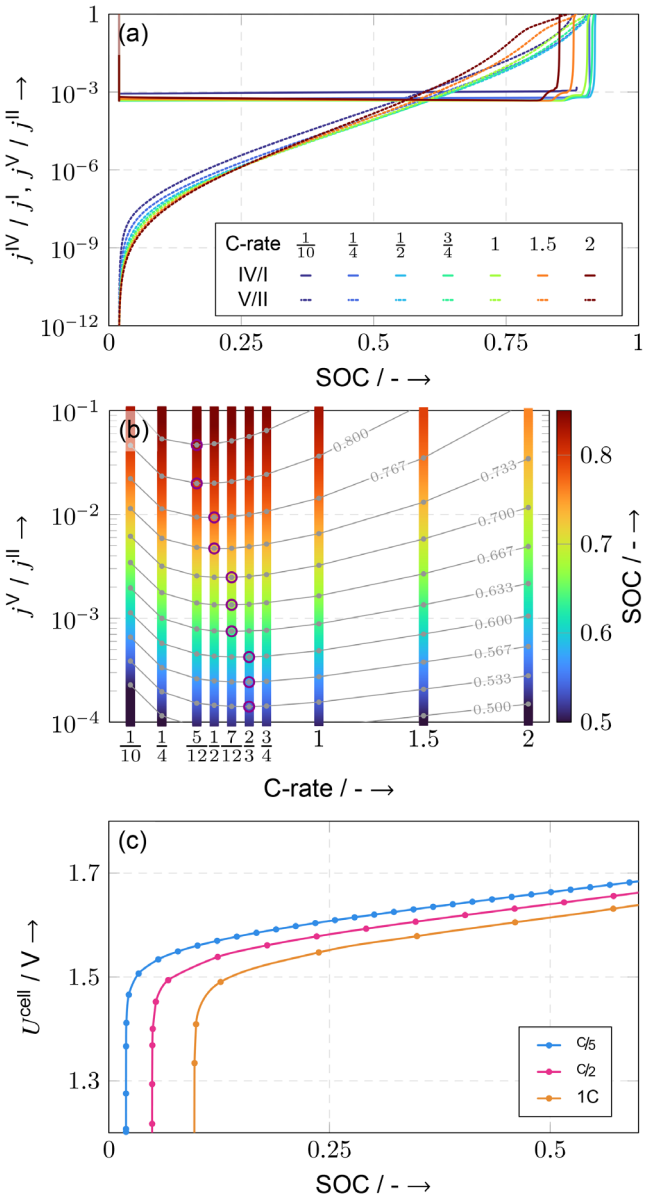

Figure 11. a) Influence of charging rate on the competition between side and main reactions. While the ratio of Reaction (5) to Reaction (1) (solid lines) stays approximately constant and on a low level, the ratio of Reaction (6) to Reaction (2) (dotted lines) changes strongly. Both show an optimal rate at which the influence of the side reaction is the lowest. b) Analysis of the ratio Reaction (6) to Reaction (2). There are optimal charging rates to minimize the influence of the OER. Gray contour lines are drawn along constant SOC (linearly interpolated between points). Based on the discrete data, the violet circles indicate charging rates with minimal influence of the side reaction. c) Cell voltage at the end of discharge over SOC (spline through data points). Lower discharging rates allow a deeper discharge.

Research Article
doi.org/10.1002/batt.202500704
Chemistry Europe
European Chemical Societies Publishing

Analyzing this rate dependence further in Figure 11b, the previous observations are visible in more detail. We see the development of the ratio of the reaction rates V/II for different C-rates along an ascending SOC. From the color scheme, and even more from the contour lines derived from it along constant SOCs, we see more clearly than before that the optimal charging rate for minimum O_2 production slowly shifts to lower C-rates with increasing SOC. Thus, a step-by-step reduction of the current during the charging operation may slow down the OER additionally.

Lastly, in Figure 11c, another optimization approach is revealed for the discharge operation. There, we see that slower discharge rates allow for a larger discharge depth. This phenomenon stems from the competition between proton diffusion speed within Ni particles, as visible in Figure S8c, Supporting Information, and the insertion/extraction reaction rate. In this sense, lowering the C-rate toward the end of discharge allows the solid diffusion in the particles to keep up with the reaction rate. This lowers the insertion rate of protons, giving them more time to diffuse toward the particle centers, which delays reaching the proton capacity in the outer shell and hence the collapse of the cell voltage. Therefore, this effect may be used to either further extent the cycle life by shifting the SOC window away from OER dominance or to increase the cycled capacity.

These observations now suggest the use of tailored C-rates and charging limits to improve the efficiency, cycle life or available capacity of the cell by adapting the cycling protocol. This is another optimization strategy in addition to the use of additives for OER suppression mentioned at the beginning.

The two approaches are now compared to the reference case from the previous sections in six different scenarios, where only the first one deals with an additive-induced reduction of the OER rate and the five remaining cover a step-wise adaption of the cycling protocol to explore the potential for cycle life and capacity improvements. These adapted cycling protocols are listed in **Table 2** and the results are shown in **Figure 12**.

Table 2. Cycling protocols analyzed. The green and red double arrows indicate the charging and discharging operations, respectively. Scenario I is the reduction of the OER rate through additives.

Sce.	Operations
II	⇒ CC| $^{C}/_{2}$ → 1.91 V » CV| 1.91 V → 8.0 Ah
	⇐ CC| 1C → 1.000 V
III	⇒ CC| $^{C}/_{2}$ → 1.91 V » CV| 1.91 V → 8.4 Ah
	⇐ CC| 1C → 1.000 V
IV	⇒ CC| $^{2C}/_{3}$ → 5.0 Ah » CC|$^{7C}/_{12}$ → 6.2 Ah » CC| $^{C}/_{2}$ → 1.91 V » CV| 1.91 V → 8.4 Ah
	⇐ CC| 1C → 1.000 V
V	⇒ CC| $^{C}/_{2}$ → 1.91 V » CV| 1.91 V → 9.2 Ah
	⇐ CC| 1C → 1.525 V » CC| $^{C}/_{2}$ → 1.500 V » CC| $^{C}/_{5}$ → 1.000 V
VI	⇒ CC| $^{2C}/_{3}$ → 6.0 Ah » CC| $^{7C}/_{12}$ → 7.2 Ah » CC| $^{C}/_{2}$ → 1.91 V » CV| 1.91 V → 9.2 Ah
	⇐ CC| 1C → 1.525 V » CC| $^{C}/_{2}$ → 1.500 V » CC| $^{C}/_{5}$ → 1.000 V

In the first two scenarios, the base assumptions are tested. Scenario I (cyan) uses the same cycling protocol as the reference simulation (blue), but uses a 50% reduced OER rate constant. Scenario II (green) does not change any reaction rate constants but examines whether the postulated advantage of intermediate C-rates has an observable influence. For this purpose, the charging current is reduced to $^{C}/_{2}$ as suggested by Figure 11a, which then also needs an adaption of the upper voltage limit to reach the CV phase before the 8 Ah limit is attained. It is reduced to 1.91 V. The discharge procedure is untouched.

In Figure 12a, we see that the cell voltage curves are not too different from the reference case for these two scenarios. Scenario I, using the same cycling protocol, is nearly congruent to the base scenario, and scenario II features a lowered charging branch due to the reduced charging speed. Visible differences arise in Figure 12b, where both scenarios have a higher CE (99.80% and 99.72%) than the reference's 99.60% (solid lines), which also reflects in a slower permanent conversion of ZnO (dashed lines) to Zn (dotted lines). These two quantities are depicted as volume-averaged volume fraction in the anode, evaluated at the end of charge, when ZnO (and subsequent zincate) shortage has the most severe influence.

Based on this enhancement of the CE, we explore now whether this may also be translated to a gain in capacity by pushing the end-of-charge limit to 8.4 Ah. Scenario III (olive) differs from scenario II just by changing this limit. Scenario IV (orange) modifies additionally the charging behavior by trying to implement a step-wise change of charging rate to stay in an optimum as suggested by Figure 11b. The discharge procedure is still untouched.

The cell voltage curves in Figure 12a feature the enlarged transferred charge and, in the case of scenario IV, the now staircase-shaped charging branch due to the step-wise switching of charging currents when specific amounts of charge have been transferred. The slightly augmented capacity lets the CE drop noticeably to around 99.41% for both, as depicted in Figure 12b, below the projected minimum of 99.5%. Thus, the continued reduction of ZnO volume fraction is accelerated compared to the base scenario, which also reflects in an accelerated degradation starting between cycles 130 and 150 as visible from the CE.

In a last step, the findings of Figure 11c are integrated into the discharge phase of the cycling protocol. For this purpose, scenarios V (purple) and VI (pink) are derived from III and IV, respectively, by adapting the discharge current to $^{C}/_{2}$ when 1.525V is underrun and subsequently to $^{C}/_{5}$ when cell voltage falls below 1.5 V. For scenario VI, the switching points for the charging current are slightly adapted to the new use-case, see Table 2. In the same step, the end-of-charge limit is again raised, now to 9.2 Ah, to make use of the anticipated capacity accessed by deep discharge.

The alteration of the cycling protocols are clearly visible in the cell voltage curves of Figure 12a: Both scenarios have an important increase of the charging phase allowing more charge to be transferred, and the discharge branch shows the two switching points of discharge current with the resulting changes in cell

Research Article
doi.org/10.1002/batt.202500704
Chemistry Europe
European Chemical Societies Publishing

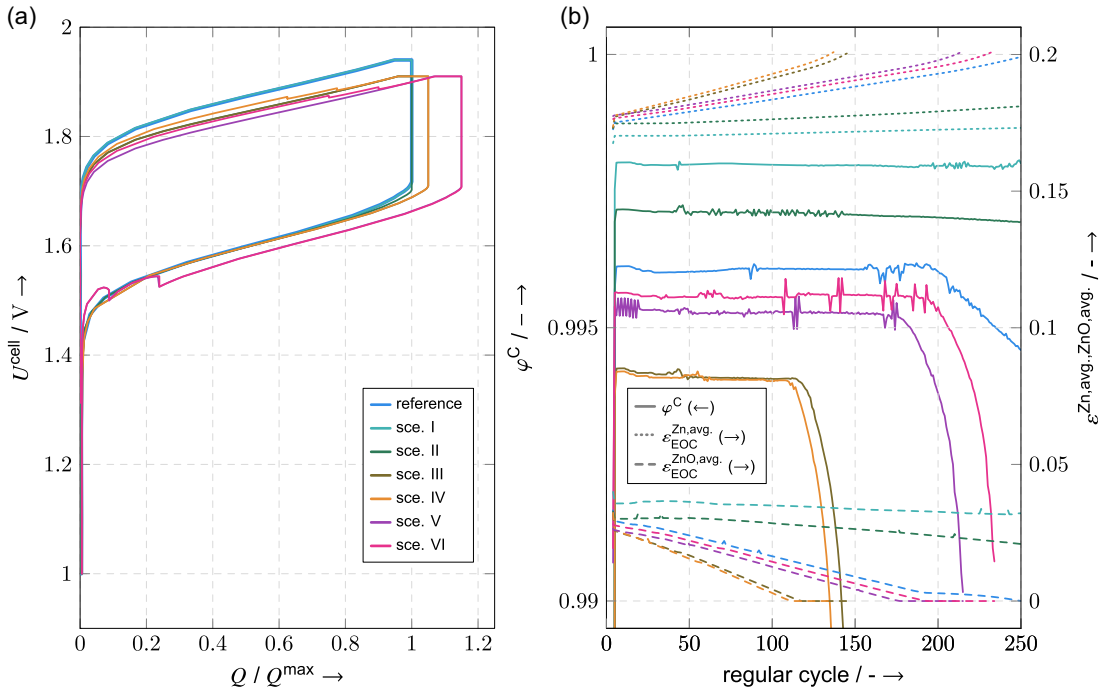

Figure 12. a) Cell voltage during the 25th regular cycle for the reference and derived scenarios and b) evolution of the Coulombic efficiency and volume-averaged Zn/ZnO volume fractions (at end of charge) over the cycle number with the same colors as in (a). Curves depicted up to the cycle where capacity fading starts.

voltage. Furthermore, the cycling to lower SOCs shifts the cell voltage curves down to lower voltages visible in the charge and discharge branches. For scenario VI, the charging branch is again staircase-shaped due to the changes in charging currents. This changed cycling regime shows nearly as good efficiencies for both scenarios as for the reference simulation (99.52% and 99.56%), see Figure 12b, with scenario VI being slightly closer. As usual, this translates equally to the conversion of ZnO to Zn with progressing cycling, which happens with the same tendencies close to that of the base scenario.

The scenarios show that a reduction of the OER rate, as well as a considered choice of cycling protocol, may improve CE, despite the reference simulation's cycling protocol being already quite good. This may be translated into either an increased cycle life or greater capacity utilization.

Scenario I is easily explained: By keeping the standard cycling protocol, the reduced reaction rate constant lowers the amount of charge being used for oxygen formation, rendering the whole process more efficient. This reduces the imbalance between charging and discharging operation, slowing down the conversion of ZnO to Zn and hence will delay the initiation of cell death by ZnO and zincate shortage. As already mentioned, this type of OER suppression is linked to the use of expensive additives like cobalt and thus not always an option. Therefore, it is noteworthy that similar improvements in CE can be achieved through a thoughtful choice of the cycle protocol, as demonstrated by scenario II. The use of intermediate charging rates, as implied by Figure 11a, indeed has a beneficial effect on the competition between OER and proton insertion/extraction reaction. As indicated by the development of the volume-averaged Zn and ZnO curves in Figure 12b, this will also lead to an extended cycle life.

The examination of scenario III reveals that these gains in efficiency and thus cycle life are only possible in a narrow corridor of arrangements. Enhancing capacity in particular means walking a fine line between improvement and deterioration. Increasing the utilized capacity by 5% to 8.4 Ah extents the accelerated oxygen formation period to such lengths that the CE drops by ≈0.3%, which is already enough to approximately halve the cycle life and thus not justifying the modest increase in capacity. The attempt to overcome this strong reduction of CE with scenario IV by using optimal charging rates as suggested by Figure 11b does not yield any change in the performance metrics.

But the integration of adapted discharge C-rates, as discussed on grounds of Figure 11c, proves that larger capacities may be accessed. Both scenarios, V and VI, show nearly as good CE as the reference simulation, with VI and its adapting charging rates being slightly ahead. This might be surprising having the nearly identical outcome of scenarios III and IV in mind, but for this scenario, the switching points for charging currents were adapted to the deep discharge in this scenario. These new switching points seem to match better the predicted OER suppressing behavior in Figure 11b. At the same time, both scenarios enable the Ni/Zn cell to use 15% more capacity by only conceding a small amount of cycle life. The larger part of this improvement is possible due to decreasing the lower SOC limit from the reference case's ≈9.5% (cf. Figure 8c) to now ≈2.3%.

Generally, we see that a careful combination of cycling operations allows access to additional performance of the cell, if lower and changing C-rates are acceptable in the cell's use-case. The exemplary scenarios showed that this may be used for extended cycle life or larger capacity usage. But also combinations of both are possible, e.g., by using scenario VI and increasing the capacity by only 12.5% which would translate to a cycled capacity of 9.0 Ah and an efficiency of about 99.65%. Furthermore, an even more thoroughly chosen set of switching points for the charge and discharge C-rates of scenarios IV and VI could exploit the potential of the optimization approaches presented here even better. The more easily accessible capacity seems to be that of the lower SOC range, where nearly 1 Ah are added in case of scenario VI compared to only 0.2 Ah in the upper SOC range.

These rather theoretical findings should, in principle, be applicable to physical Ni/Zn cells as well. While finding e.g., optimal switching points for C-rates could be a tedious work and exploiting deep discharge regions too much could lead to e.g., cracking of the Ni electrode due to volume expansion, leading to a reduced cycle life, the careful exploration of these cycling protocol optimization strategies may increase the capacity and/or cycle life by several percent, making Ni/Zn cells more competitive.

4. Conclusion

A physico-chemical, volume-averaged, 3D model of a Ni/Zn cell with additional focus on side reactions and active material particles was presented. The former includes, besides the important OER and HER, a rudimentary implementation of O_2 and H_2 outgassing and O_2 recombination with Zn. The latter comprises hindered transport due to ZnO precipitation around Zn particles as well as solid diffusion of inserted H^+ in Ni active material.

The model has been adjusted to experimental data of a prototypical Ni/Zn cell, and computational studies have been conducted to compare the behavior of the virtual twin. Through 3D simulation and comparison to μ-XRF data of the prototypical cell, it has been shown that the model is capable of reproducing the zinc shape change effect. Analyzing the convective flow throughout a cycle revealed that density changes of the electrolyte solution due to variations in the hydroxide and zincate concentration surpass pore volume changes due to Zn dissolution/deposition and ZnO precipitation/dissolution. Hence, electrolyte solution is counter-intuitively pressed out of the Zn electrode during charging, while it is sucked back in during discharge. This pattern may assist the zinc shape change through convecting zincate in waves toward the center of the electrode, as it already was pointed out by experiments in literature.

Analysis of long-term cycling simulations revealed that Zn/ZnO imbalance in each cycle is a primary cause of cell failure at low- and mid-range cycle numbers. This imbalance, which manifests as insufficient CE, stems from progressive depletion of ZnO and ultimately $Zn(OH)_4^{2-}$. The underlying cause is the OER, which becomes increasingly active at higher states of charge.

Based on these insights, two key optimization strategies for extending cycle life have been identified. The first approach involves using additives such as cobalt to manipulate the standard reduction potential of the OER, thereby slowing the detrimental reaction. Alternatively, the cycling protocol may be modified to exploit an observed C-rate dependence of the competition between insertion reaction and OER. This second strategy offers the attractive possibility of avoiding additives like Co by optimizing the cycling protocol, requiring only careful selection of appropriate C-rates and usable capacity ranges. As demonstrated, this approach is also suitable to boost the cycle life and cycled capacity considerably.

Supporting Information

The authors have cited additional references within the Electronic Supplementary Information.[49,65–138]

Acknowledgements

This work is supported by the European Union's Horizon 2020 research and innovation programme under grant agreement no 963576 (LoLaBat) and by the Franco-German project ZABSES, co-funded by the Agence Nationale de la Recherche (ANR, ANR-22-MER3-0005-02) and the Federal Ministry of Education and Research of Germany (BMBF, 03XP0505A). The authors acknowledge support by the state of Baden-Württemberg through bwHPC and the German Research Foundation (DFG) through grant no INST 40/5751 FUGG (JUSTUS 2 cluster). Emanuele Marini (ZSW) is acknowledged for the acquisition of the μ-XRF experimental data.

Open Access funding enabled and organized by Projekt DEAL.

Conflict of Interest

The authors declare no conflict of interest.

Author Contributions

Felix K. Schwab: conceptualization (lead); formal analysis (lead); methodology (lead); software (lead); validation (lead); visualization (lead); writing—original draft (lead); writing—review & editing (equal). **Britta Doppl**: conceptualization (supporting); methodology (supporting); writing—review & editing (equal). **Niklas J. Herrmann**: conceptualization (supporting). **Alice Boudet**: investigation (equal); validation (supporting); writing—review & editing (equal). **Shadi Mirhashemi**: funding acquisition (equal); investigation (equal); validation (supporting); writing—review & editing (equal). **Sylvain Brimaud**: funding acquisition (equal); investigation (equal); validation (supporting); writing—review & editing (equal). **Birger Horstmann**: conceptualization (supporting); funding acquisition (equal); supervision (lead); writing—review & editing

(equal). **Felix K. Schwab** and **Britta Doppl** contributed equally to this work.

Data Availability Statement

The data that support the findings of this study are available from the corresponding author upon reasonable request.

Keywords: concentrated solution theory · continuum model · nickel-zinc battery · volume averaged · zinc shape change

[1] S. Clark, N. Borchers, Z. Jusys, R. J. Behm, B. Horstmann, *Encyclopedia of Electrochemistry*, Wiley-VCH Verlag GmbH & Co. KGaA, Weinheim **2020**, pp. 1–54.
[2] N. Borchers, S. Clark, B. Horstmann, K. Jayasayee, M. Juel, P. Stevens, *J. Power Sources* **2021**, *484*, 229309.
[3] Y. Liang, Y. Yao, *Nat. Rev. Mater.* **2023**, *8*, 109.
[4] X. Zhang, *Encyclopedia of Electrochemical Power Sources* (Ed: J. Garche), Elsevier, Amsterdam **2009**, pp. 454–468.
[5] T. B. Reddy, *Linden's Handbook of Batteries*, 4th ed., McGrawHill Education, New York, NY **2010**.
[6] N. J. Herrmann, H. Euchner, A. Groß, B. Horstmann, *Adv. Energy Mater.* **2024**, *14*, 2302553.
[7] N. J. Herrmann, B. Horstmann, *Energy Storage Mater.* **2024**, *70*, 103437.
[8] F. R. McLarnon, E. J. Cairns, *J. Electrochem. Soc.* **1991**, *138*, 645.
[9] A. R. Mainar, O. Leonet, M. Bengoechea, I. Boyano, I. de Meatza, A. Kvasha, A. Guerfi, J. Alberto Blázquez, *Int. J. Energy Res.* **2016**, *40*, 1032.
[10] W. Lu, C. Zhang, H. Zhang, X. Li, *ACS Energy Lett.* **2021**, *6*, 2765.
[11] A. Naveed, T. Rasheed, B. Raza, J. Chen, J. Yang, N. Yanna, J. Wang, *Energy Storage Mater.* **2022**, *44*, 206.
[12] A. Shukla, S. Venugopalan, B. Hariprakash, *J. Power Sources* **2001**, *100*, 125.
[13] J.-Y. Huot, in *Encyclopedia of Electrochemical Power Sources* (Ed: J. Garche), Elsevier, Amsterdam **2009**, pp. 883–892.
[14] K. Bogomolov, Y. Ein-Eli, *ChemSusChem* **2024**, *17*, e202300940.
[15] D. Reisner, M. Eisenberg, in *Proc. 24th Intersociety Energy Conversion Engineering Conf., Washington, DC*, Vol. *3*, IEEE **1989**, pp. 1677–1682.
[16] D. E. Turney, J. W. Gallaway, G. G. Yadav, R. Ramirez, M. Nyce, S. Banerjee, Y.-C. K. Chen-Wiegart, J. Wang, M. J. D'Ambrose, S. Kolhekar, J. Huang, X. Wei, *Chem. Mater.* **2017**, *29*, 4819.
[17] J. Jindra, *J. Power Sources* **1992**, *37*, 297.
[18] J. McBreen, *J. Power Sources* **1994**, *51*, 37.
[19] E. J. Podlaha, H. Y. Cheh, *J. Electrochem. Soc.* **1994**, *141*, 15.
[20] J. Wen, H. Li, Y. Han, Z. Feng, L. Zhang, H. Liu, S. Sheng, *Electrochim. Acta* **2022**, *428*, 140899.
[21] K. W. Choi, D. N. Bennion, J. Newman, *J. Electrochem. Soc.* **1976**, *123*, 1616.
[22] W. G. Sunu, D. N. Bennion, *J. Electrochem. Soc.* **1980**, *127*, 2007.
[23] J. Chen, H. Y. Cheh, *J. Electrochem. Soc.* **1993**, *140*, 1213.
[24] E. Deiss, F. Holzer, O. Haas, *Electrochim. Acta* **2002**, *47*, 3995.
[25] Z. Mao, R. E. White, *J. Electrochem. Soc.* **1992**, *139*, 1105.
[26] J. Stamm, A. Varzi, A. Latz, B. Horstmann, *J. Power Sources* **2017**, *360*, 136.
[27] T. Schmitt, T. Arlt, I. Manke, A. Latz, B. Horstmann, *J. Power Sources* **2019**, *432*, 119.
[28] D. Fan, R. E. White, *J. Electrochem. Soc.* **1991**, *138*, 2952.
[29] B. Paxton, J. Newman, *J. Electrochem. Soc.* **1997**, *144*, 3818.
[30] W. Gu, C. Wang, S. Li, M. Geng, B. Liaw, *Electrochim. Acta* **1999**, *44*, 4525.
[31] Y. Pan, V. Srinivasan, C. Wang, *J. Power Sources* **2002**, *112*, 298.
[32] P. Albertus, J. Christensen, J. Newman, *J. Electrochem. Soc.* **2007**, *155*, A48.
[33] Z. Mao, P. D. Vidts, R. E. White, J. Newman, *J. Electrochem. Soc.* **1994**, *141*, 54.
[34] P. D. Vidts, R. E. White, *J. Electrochem. Soc.* **1995**, *142*, 1509.
[35] K. W. Choi, N. P. Yao, in *Proc. Symp. On Battery Design and Optimization*, Vol. *79* (Ed: S. Gross), The Electrochemical Society, Inc., Princeton, NJ **1979**, pp. 62–80.
[36] K. G. Miller, F. R. McLarnon, E. J. Cairns, *The Electrochemical Society Extended Abstracts*, Vol. *88*, The Electrochemical Society, Inc., Pennington, NJ **1988**, p. 8.
[37] M. J. Isaacson, F. R. McLarnon, E. J. Cairns, *J. Electrochem. Soc.* **1990**, *137*, 2014.
[38] I. Arise, S. Kawai, Y. Fukunaka, F. R. McLarnon, *J. Electrochem. Soc.* **2009**, *157*, A171.
[39] I. Arise, S. Kawai, Y. Fukunaka, F. R. McLarnon, *J. Electrochem. Soc.* **2012**, *160*, D66.
[40] C. Huang, A. Armutlulu, M. G. Allen, S. A. B. Allen, *J. Power Sources* **2017**, *358*, 101.
[41] A. Latz, J. Zausch, *J. Power Sources* **2011**, *196*, 3296.
[42] A. Latz, J. Zausch, *Beilstein J. Nanotechnol.* **2015**, *6*, 987.
[43] B. Doppl, F. K. Schwab, N. J. Herrmann, B. Horstmann, Modeling the Influence of Zinc Particlesize on Gas Evolution in Secondary Nickel-Zinc Battery Cells, to be submitted.
[44] M. Schammer, B. Horstmann, A. Latz, *J. Electrochem. Soc.* **2021**, *168*, 026511.
[45] F. Kilchert, M. Lorenz, M. Schammer, P. Nürnberg, M. Schönhoff, A. Latz, B. Horstmann, *Phys. Chem. Chem. Phys.* **2023**, *25*, 25965.
[46] B. Tjaden, S. J. Cooper, D. J. Brett, D. Kramer, P. R. Shearing, *Curr. Opin. Chem. Eng.* **2016**, *12*, 44, nanotechnology/Separation Engineering.
[47] Fraunhofer ITWM, BEST, https://www.itwm.fraunhofer.de/en/departments/sms/products-services/best-battery-electrochemistry-simulation-tool.html.
[48] Frauenhofer SCAI, SAMG, https://www.scai.fraunhofer.de/en/business-research-areas/fast-solvers/products/samg.html.
[49] T. Schmitt, A. Latz, B. Horstmann, *Electrochim. Acta* **2020**, *333*, 135491.
[50] H. Childs, E. Brugger, B. Whitlock, J. Meredith, S. Ahern, K. Bonnell, M. Miller, G. Weber, C. Harrison, D. Pugmire, T. Fogal, C. Garth, A. Sanderson, E. W. Bethel, M. Durant, D. Camp, J. Favre, O. Rübel, P. Navratil, F. Vivodtzev, in *High Performance Visualization – Enabling Extreme Scale Scientific Insight, Chapter Visit: An End-User Tool for Visualizing and Analyzing Very Large Data*, Chapman and Hall/CRC Press, Boca Raton, FL **2012**, pp. 357–372.
[51] Lawrence Livermore National Laboratory, VisIt (Version 3.3.3), https://visit-dav.github.io/visit-website/index.html.
[52] D. Eberle, B. Horstmann, *Electrochim. Acta* **2014**, *137*, 714.
[53] K. P. Ta, J. Newman, *J. Electrochem. Soc.* **1999**, *146*, 2769.
[54] V. Srinivasan, J. W. Weidner, R. E. White, *J. Solid State Electrochem.* **2000**, *4*, 367.
[55] V. Srinivasan, J. W. Weidner, J. Newman, *J. Electrochem. Soc.* **2001**, *148*, A969.
[56] M. Casas-Cabanas, M. D. Radin, J. Kim, C. P. Grey, A. Van der Ven, M. R. Palacín, *J. Mater. Chem. A* **2018**, *6*, 19256.
[57] J. Börjesson Axén, *Ph.D. Thesis*, KTH, Applied Electrochemistry, Stockholm **2023**.
[58] R. E. F. Einerhand, W. Visscher, J. J. M. de Goeij, E. Barendrecht, *J. Electrochem. Soc.* **1991**, *138*, 1.
[59] R. E. F. Einerhand, W. Visscher, J. J. M. de Goeij, E. Barendrecht, *J. Electrochem. Soc.* **1991**, *138*, 7.
[60] J. McBreen, *J. Electrochem. Soc.* **1972**, *119*, 1620.
[61] J. McBreen, E. J. Cairns, in *Advances in Electrochemistry and Electrochemical Engineering* (Eds: H. Gerischer, C. W. Tobias), John Wiley & Sons, Inc., New York, NY **1978**, pp. 273–352.
[62] R. G. Gunther, R. M. Bendert, *J. Electrochem. Soc.* **1987**, *134*, 782.
[63] V. Caldeira, R. Rouget, F. Fourgeot, J. Thiel, F. Lacoste, L. Dubau, M. Chatenet, *J. Power Sources* **2017**, *350*, 109.
[64] J. Hendrikx, W. Visscher, E. Barendrecht, *J. Appl. Electrochem.* **1986**, *16*, 175.
[65] B. Horstmann, A. Latz, F. K. Schwab, in *Encyclope-Dia of Electrochemical Power Sources*, 2nd ed. (Ed: J. Garche), Elsevier, Oxford **2025**, pp. 186–199.
[66] J. Newman, N. P. Balsara, *Electrochemical Systems, The Electrochemical Society Series*, 4th ed., Wiley, Hoboken, NJ **2021**.
[67] L. J. Bolay, T. Schmitt, S. Hein, O. S. Mendoza-Hernandez, E. Hosono, D. Asakura, K. Kinoshita, H. Matsuda, M. Umeda, Y. Sone, A. Latz, B. Horstmann, *J. Power Sources Adv.* **2022**, *14*, 100083.
[68] SunErgy, private communication, unpublished.
[69] Cergy Paris Université, private communication, unpublished.
[70] ZSW, private communication, unpublished.
[71] M.-B. Liu, G. M. Cook, N. P. Yao, *J. Electrochem. Soc.* **1981**, *128*, 1663.
[72] Q. C. Horn, Y. Shao-Horn, *J. Electrochem. Soc.* **2003**, *150*, A652.
[73] R. A. Matula, *J. Phys. Chem. Ref. Data* **1979**, *8*, 1147.
[74] P. H. Miller, *Phys. Rev.* **1941**, *60*, 890.
[75] G. T. Meaden, *Electrical Resistance of Metals*, Springer US, Boston, MA **1965**.
[76] V. G. Orlov, A. A. Bush, S. A. Ivanov, V. V. Zhurov, *J. Low Temp. Phys.* **1996**, *105*, 1541.

[77] F. Freund, H. Wengeler, *Ber. Bunsen-Ges. Phys. Chem.* **1980**, *84*, 866.
[78] Y. Nishi, S. Iizuka, M. C. Faudree, R. Oyama, *Mater. Trans.* **2012**, *53*, 940.
[79] H. O. Pierson, *Handbook of Refractory Carbides and Nitrides: Properties, Characteristics, Processing, and Applications*, Noyes Publications, Westwood, NJ **1996**.
[80] S. Motupally, C. C. Streinz, J. W. Weidner, *Journal of The Electrochemical Society* **1995**, *142*, 1401.
[81] R. N. Bhatia, K. E. Gubbins, R. D. Walker, *Trans. Faraday Soc.* **1968**, *64*, 2091.
[82] C. E. May, H. E. Kautz, in *Technical Report at 154th Electrochemical Society Meeting* **1978**, p. 20.
[83] J. Dean, N. Lange, *Lange's Handbook of Chemistry*, 15th ed., McGraw-Hill, New York, NY **1999**.
[84] M. Liu, B. R. Faulds, G. M. Cook, N. P. Yao, *J. Electrochem. Soc.* **1981**, *128*, 2049.
[85] J. Barthel, W. Kunz, P. Turq, O. Bernard, in *Encyclopedia of Physical Science and Technology*, 3rd ed. (Ed: R. A. Meyers), Academic Press, New York, NY **2003**, pp. 243–259.
[86] P. Atkins, J. de Paula, *Atkins' Physical Chemistry*, 8th ed., W. H. Freeman and Company, New York, NY **2006**.
[87] D. M. See, R. E. White, *J. Chem. Eng. Data* **1997**, *42*, 1266.
[88] A. Katchalsky, P. F. Curran, *Nonequilibrium Thermodynamics in Biophysics*, Harvard University Press, Cambridge, MA and London, England **1965**.
[89] K. D. Fong, H. K. Bergstrom, B. D. McCloskey, K. K. Mandadapu, *AIChE J.* **2020**, *66*, e17091.
[90] K. Malaie, F. Scholz, U. Schröder, *ChemElectroChem* **2023**, *10*, e202201118.
[91] W. G. Sunu, *Phd Thesis*, University of California, Los Angeles, CA **1978**.
[92] D. N. Bennion, *Phd Thesis*, University of California, Berkeley, CA **1964**.
[93] M. I. Usanovich, T. I. Sushkevich, *Zh. Prikl. Khim.* **1951**, *24*, 590.
[94] R. Gilliam, J. Graydon, D. Kirk, S. Thorpe, *Int. J. Hydrogen Energy* **2007**, *32*, 359.
[95] W. H. Dyson, L. A. Schreier, W. P. Sholette, A. J. Salkind, *J. Electrochem. Soc.* **1968**, *115*, 566.
[96] A. A. Lang, *Phd Thesis*, University of Western Ontario, London, ON **1956**.
[97] A. Himy, *Silver-Zinc Battery: Phenomena and Design Principles*, Vantage Press, Inc., New York, NY **1986**.
[98] D. Trudgeon, *Phd Thesis*, University of Exeter, Exeter, UK **2019**.
[99] K. Takahashi, *Corros. Eng.* **1974**, *23*, 557.
[100] J. Kriegsmann, H. Cheh, *J. Power Sources* **1999**, *84*, 52.
[101] D. M. See, R. E. White, *J. Chem. Eng. Data* **1998**, *43*, 986.
[102] S. U. Falk, A. J. Salkind, *Alkaline Storage Batteries, The Electrochemical Society Series*, John Wiley & Sons, New York, NY **1969**.
[103] J. McBreen, Study to Investigate and Improve the Zinc Electrode for Spacecraft Electrochemical Cells, Contractor Report NASA-CR-92599, Yardney Electric Corp., New York, NY **1967**.
[104] T. P. Dirkse, in *Power Sources 3; Research and Development in Non-Mechanical Electrical Power Sources: Proc. 7th Int. Symp.* (Ed: D. H. Collins), Oriel Press, Newcastle Upon Tyne, UK **1970**, pp. 485–493.
[105] J. L. Gendler, *Master's Thesis*, University of Pennsylvania, Philadelphia, PA **1976**, https://apps.dtic.mil/sti/tr/pdf/ADA052807.pdf.
[106] L. Nanis, Study of zinc-silver oxide battery system, Contractor Report NASA-CR-109347, California Institute of Technology **1970**.
[107] H. J. De Wane, W. J. Hamer, Electrochemical data. Part 10 - Electrolytic conductivity of aqueous solutions of the alkali metal hydroxides, Contractor Report NASA-CR-97593, National Bureau of Standards Washington **1968**.
[108] D. P. Trudgeon, X. Li, *Electrochim. Acta* **2021**, *367*, 137479.
[109] G. Akerlof, P. Bender, *J. Am. Chem. Soc.* **1941**, *63*, 1085.
[110] V. Yushkevich, I. Maksimova, V. Bullan, *Elektrokhimiya* **1967**, *3*, 1491.
[111] S. Lengyel, J. Giber, G. Beke, A. Vértes, *Acta Chim. Hung. Tomus* **1963**, *39*, 357.
[112] E. L. Cussler, *Diffusion: Mass Transfer in Fluid Systems, Cambridge Series in Chemical Engineering*, Cambridge University Press, Cambridge, UK **2009**.
[113] M. J. Tham, R. D. J. Walker, K. E. Gubbins, *J. Phys. Chemistry* **1970**, *74*, 1747.
[114] A. Hodges, S. Renz, F. Lohmann-Richters, A. AlMusawi, A. Jupke, W. Lehnert, G. F. Swiegers, G. G. Wallace, *J. Chem. Eng. Data* **2023**, *68*, 1485.
[115] A. Kube, N. Wagner, K. A. Friedrich, *J. Electrochem. Soc.* **2021**, *168*, 050531.
[116] M. A. Klochko, M. M. Godneva, *Zh. Neorg. Khim.* **1959**, *4*, 2127.
[117] I. D. Zaytsev, G. G. Asayev, *Properties of Aqueous Solutions of Electrolytes*, CRC Press, Boca Raton, FL **1992**.
[118] Y. Jie Guo, H. Bin Xu, F. Guo, S. Li Zheng, Y. Zhang, *Trans. Nonferrous Met. Soc. China* **2010**, *20*, s32.
[119] S. Siu, J. W. Evans, *J. Electrochem. Soc.* **1997**, *144*, 1278.
[120] G. W. Jackson, D. F. James, *Can. J. Chem. Eng.* **1986**, *64*, 364.
[121] J. Bear, *Dynamics of Fluids in Porous Media*, Dover Publications, New York, NY **1972**.
[122] J. Kozeny, *Sitzungsber. Akad. Wiss. Math.-Naturwiss. Kl.* **1927**, *136*, 271.
[123] P. Carman, *Trans. Inst. Chem. Eng.* **1937**, *15*, 150.
[124] K. Feldkamp, *Chem. Ing. Tech.* **1969**, *41*, 1181.
[125] J. Blazy, R. Blazy, *Case Stud. Constr. Mater.* **2021**, *14*, e00549.
[126] R. S. Yeo, Research on Separators for Alkaline Zinc Batteries: Final Report, Contractor Report AC0376SF00098, Pinnacle Research Institute **1985**.
[127] M. Leverett, *Trans. AIME* **1941**, *142*, 152.
[128] T. Danner, B. Horstmann, D. Wittmaier, N. Wagner, W. G. Bessler, *J. Power Sources* **2014**, *264*, 320.
[129] S. Foroughi, B. Bijeljic, M. J. Blunt, *Transp. Porous Media* **2022**, *145*, 683.
[130] T. Schmitt, *Phd Thesis*, University of Ulm, Ulm, Germany **2020**.
[131] K. Watanabe, N. Kumagai, *J. Power Sources* **1997**, *66*, 121.
[132] K. Watanabe, N. Kumagai, *J. Power Sources* **1998**, *76*, 167.
[133] J. O. Bockris, Z. Nagy, A. Damjanovic, *J. Electrochem. Soc.* **1972**, *119*, 285.
[134] A. J. Bard, L. R. Faulkner, *Electrochemical Methods: Fundamentals and Applications*, 2nd ed., John Wiley & Sons, New York, NY **2000**.
[135] *CRC Handbook of Chemistry and Physics*, 85th ed. (Ed: D. R. Lide), CRC Press, Boca Raton, FL **2005**.
[136] J. Hendrikx, A. van der Putten, W. Visscher, E. Barendrecht, *Electrochim. Acta* **1984**, *29*, 81.
[137] R. Jain, T. C. Adler, F. R. McLarnon, E. J. Cairns, *J. Appl. Electrochem.* **1992**, *22*, 1039.
[138] J. C. Moore, R. Battino, T. R. Rettich, Y. P. Handa, E. Wilhelm, *J. Chem. Eng. Data* **1982**, *27*, 22.

Manuscript received: September 8, 2025
Revised manuscript received: October 31, 2025
Version of record online: